Interaction of a Deformable Solid with Two-Phase Flows: An Eulerian based Numerical Model for Fluid-Structure Interaction using the Level Contour Reconstruction Method

Seungwon Shin, Jalel Chergui, Damir Juric

Interaction of a Deformable Solid with Two-Phase Flows: An Eulerian based Numerical Model for Fluid-Structure Interaction using the Level Contour Reconstruction Method

Seungwon Shin[1*], Jalel Chergui[2] and Damir Juric[2]

[1] Department of Mechanical and System Design Engineering

Hongik University

Seoul, 121-791 Korea

[2] Laboratoire d'Informatique pour la Mécanique et les Sciences de l'Ingénieur (LIMSI),

Centre National de la Recherche Scientifique (CNRS),

Université Paris Saclay, Bât. 507, Rue de Belvédère

Campus Universitaire, F-91405 Orsay, France

[*]Corresponding Author:

Seungwon Shin, PhD

Professor

Department of Mechanical and System Design Engineering

Hongik University

Sangsu-dong, 72-1, Mapo-gu

Seoul, 121-791, Korea

Phone: 82-2-320-3038

FAX: 82-2-322-7003

E-Mail: sshin@hongik.ac.kr

ABSTRACT

We describe the formulation of a method for fluid-structure interaction (FSI) involving the coupling of moving and/or flexible solid structures with multiphase flows in the framework of the Level Contour Reconstruction Method (LCRM). We present an Eulerian based numerical procedure for tracking the motion and interaction of a liquid-gas interface with a fluid-solid interface in the Lagrangian frame together with the evaluation of the fluid transport equations coupled to those for the solid transport, namely the left Cauchy-Green strain tensor field, in the Eulerian frame. To prevent excessive dissipation due to the convective nature of the solid transport equation, a simple incompressibility constraint for the strain field is enforced. A single grid structure is used for both the fluid and solid phases which allows for a simple and natural coupling of the fluid and solid dynamics. Several benchmark tests are performed to show the accuracy of the numerical method and which demonstrate accurate results compared to several of those in the existing literature. In particular we show that surface tension effects including contact line dynamics on the deforming solid phase can be properly simulated. The three-phase interaction of a droplet impacting on a flexible cantilever is investigated in detail. The simulations follow the detailed motion of the droplet impact (and subsequent deformation, breakup and fall trajectory) along with the motion of the deformable solid cantilever due to its own weight as well as due to the force of the droplet impact.

Keywords: multiphase flow; numerical simulation; front-tracking method; solid stress; Eulerian based formulation; fluid-structure interaction.

1. INTRODUCTION

Numerical simulation and analysis are being called upon to provide solutions to increasingly complex real-world engineering problems where crucial information cannot be provided by theory or experiment alone. Often these problems involve the dynamics of multiphase flows in complex geometries with additional physics due to complex rheology, interfacial physics, transport of surface-active agents, heat transport or interactions with solid structures. Here we focus on the development of a method for fluid-structure interaction involving the interaction of moving and/or flexible solid structures with multiphase flows based on the Level Contour Reconstruction Method (LCRM).

Phase interfaces can be present between either a liquid and a gas or a fluid and a solid. The numerical treatment of liquid-gas interfaces is one of the central topics of interest in the multiphase flow modeling community with attention focused on applications in engineering and physics involving interface deformation and surface tension forces. Very often, the amount of liquid-gas interface deformation is quite large. Thus, not only is an accurate interface tracking mechanism required of the numerical scheme but also an effective means of handling topology change in problems involving rupture or coalescence such as in drop/spray dynamics. The main categories of methods that have been devised to represent such interface motion are the VOF[1], Level Set[2,3] and Front Tracking[4] methods all of which use a stationary underlying Eulerian mesh structure for the solution of the bulk transport equations. The Front Tracking method differs in that it introduces an additional tracked 2D Lagrangian triangular grid which moves through the underlying 3D mesh structure. These methods were developed partly in an attempt to overcome shortcomings related to earlier approaches involving the fitting of an Eulerian mesh to the moving interface boundary which has difficulty in handling highly deforming interfaces due to the necessity of remeshing the

entire computational domain.

The numerical treatment of coupled fluid-solid motion has been the focus of research in the Fluid-Structure Interaction community. Of particular interest are highly deformable solid structures such as thin membranes and modeling of cellular structures that play a key role in many biological applications. In general, an Eulerian mesh has the advantage of describing fluid motion and a Lagrangian approach has advantages for describing the motion of a solid. However, the two grid structures are usually not compatible. Various attempts have been made to overcome this difficulty and these can be categorized as the: (1) Lagrangian-Lagrangian, (2) Lagrangian-Eulerian, (3) Eulerian-Eulerian approach for the solid and liquid, respectively. The Lagrangian-Lagrangian approach treats both the solid and fluid with Lagrangian elements which is conventional in the solid mechanics community. The Finite Element Method (FEM) is widely used for solid stress analysis and similar formulations can be defined for the fluid flow outside the solid. Since this approach can use existing and well-verified FEM formulations for the structural analysis, it has been mainly used for short simulation times or where deformation is very small. However, for larger solid deformation, the 3D grid structure has to be refreshed frequently and is thus costly and is still limited to relatively small deformations. Some variations such as the Arbitrary Lagrangian Eulerian (ALE) Finite Element Method[5] have been developed but costly and difficult remeshing of the grid is still required for significantly large deformation.

To cope with larger deformation, the Lagrangian-Eulerian approach is used. The solid deformation is treated within the regular Lagrangian framework but fluid motion is solved on an Eulerian grid which is the conventional approach in fluid dynamics. The fluid and solid problems are solved separately on their respective Eulerian and Lagrangian grids where they can be treated more effectively. An accurate communication method is necessary for the interaction between fluid and solid motion. For this the Fictitious Domain Method (FDM) or

the Immersed Boundary Method (IBM) are widely used, both of which enforce a body force due to the solid in the fluid momentum equation. For the FDM, the Navier-Stokes equations are applied to the entire simulation domain assuming that the moving solid behaves as another fluid. The rigid body constraint is enforced by applying averaged velocities in the solid region. On the other hand, the IBM uses delta function source terms at the fluid-solid boundary to enforce the necessary boundary conditions.

Baaijens[6] proposed a fictitious domain/mortar element (FD/ME) approach which is based on the fictitious domain method by Glowinski *et al* [7] to solve thin membrane movement. The FDM was used for complex or moving geometry and the solid domain was solved similarly as for the fluid. A Lagrange multiplier method, originally conceived by Glowinski *et al* [7] for deforming particulate flow, was used to enforce rigid body motion. This method has been modified by Yu[8] in a general formulation which enforces the fluid to move at the same speed as the solid.

Owing to advanced formulations of the Immersed Boundary Method (IBM), first introduced by Peskin[9], great success has been achieved for complex fluid-structure interaction problems. Zhao *et al* [10] successfully combined the Lagrangian approach for the solid and the Eulerian for the fluid by implementing the necessary body force term in the fluid momentum equation. The solid elastic stress is computed using a Finite Element method. Standard isoparametric finite-element interpolation was used to obtain the deformation tensor. To alleviate numerical instabilities arising from low order isoparametric interpolants, a super-convergent patch recovery method was utilized. Various formulations for the body force including immersed boundary or immersed interface were tested. They also formulated a force projection method to reduce the smearing effect near the interface. Momentum forcing was performed inside the solid domain after multiple subdivisions. To maintain the incompressibility condition of the solid, additional constraints were applied to the material

points. A slight modification of the method of Zhao *et al* [10] was proposed by He *et al* [11]. To represent solid motion, the Level Set function was utilized. Four types of Level Set field were generated to compute the deformation stress tensor at Eulerian grid locations. Velocity extrapolation was necessary for proper transport of the solid. The fall of a solid sphere covered by a shell of water on a horizontal pool was successfully simulated.

More complex simulations were carried out by Huang *et al* [12]. Incompressible fluid motion was computed using a fractional step method on a staggered grid and solid deformation was calculated in moving curvilinear coordinates on top of the Eulerian grid for the velocity and pressure. The energy method was used to derive the constitutive equation for the solid. Interaction between solid and fluid is enforced by the immersed boundary technique. Tian *et al* [13] combined existing immersed boundary methods with a general finite element method suitable for non-linear biological structures with large deformation. Since the finite element formulation is well benchmarked for non-linear structural problems involving general shapes and complex material behavior, a combination of the existing methods with an enhanced numerical formulation for stability was implemented. Several benchmark tests were performed to generate baselines for future numerical studies. Jiang *et al* [14] proposed a sharp-interface, immersed, smoothed finite element method (Sharp-ISFEM) which introduced a sharp interface technique into the immersed, smoothed finite element method (ISFEM) with the implementation of line normal reconstruction for unstructured grids. Computational speed was also greatly increased using an advanced search algorithm. Various three-dimensional problems such as the hovering motion of deformable wings were tested.

Several interesting variations of the IBM have also been developed. Gil *et al* [15] proposed an immersed structural potential method for FSI. The basic idea is to model the solid structure with a potential energy function. Material points inside the solid are moved with the

underlying fluid velocity as in the general IBM with specific kernel functions. Velocity gradient tensors are also interpolated directly from the Eulerian grid and computed structural stresses were distributed back to the fluid. This can minimize diffusion of the interface caused by repeated interpolation and distribution in the IBM. A more realistic viscoelastic constitutive equation was modeled for problems involving cardiovascular tissue. To increase the order of accuracy of the computation of the deformation gradient tensor, a special integration procedure was devised which can maintain the incompressibility constraint of the deformation tensor field. Some enhancements followed which utilize spline-based kernel functions and Gaussian quadrature for the interpolation/distribution procedure[16].

The methods above using IBM techniques can be very efficient since individual formulations for both fluid and solid can be utilized fully to their advantage in each phase domain. However, this still generates additional difficulty for the solid when deformation becomes severe and mesh restructuring for the solid is necessary. Usually, FEM type solutions are effective for relatively small deformation. Very recently, several attempts were made to simulate solid deformation in the full Eulerian approach. Sugiyama *et al* [17] first proposed such an Eulerian approach for the solid stress using a one equation model for both phases. The modified left Cauchy strain tensor field is advanced in time in the fully Eulerian frame. The interface is tracked by the Volume-of-fluid method. Then the Cauchy strain tensor field is filtered using the volume fraction of the solid. Several hyper-elastic materials were chosen for benchmark tests to demonstrate the accuracy of the method. Even though their method showed good performance with various hyper-elastic materials, most of their simulations were confined to cases with blunt objects where the aspect ratio in the major directions is relatively small. The movement of the solid can be large but relative deformation from the initial shape is somewhat limited. The method has been extended to three-dimensions[18] and a fully implicit formulation for the solid stress was also added to

increase the stability constraint during time advancement[19]. Esmailzadeh *et al* [20] slightly modified the method of Sugiyama *et al* [17] by increasing solid viscosity to reduce nonphysical dynamic effects at the fluid-solid interface. A modified procedure for the implicit solid stress was also introduced. The benchmark experiment of a falling elastic ball on a flat surface was performed to check the accuracy of their method. Numerical results showed good accuracy compared to experiment. Extensive parallelization of the full Eulerian scheme based on the building cube method has recently been achieved[21].

Most of the numerical studies mentioned so far are confined to multiphase problems with a single phase boundary, i.e. liquid-gas or fluid-solid. Recently, three phase problems where both liquid-gas and fluid-solid interfaces are present are being tested. Meduri *et al* [22] proposed a partitioned scheme for highly non-linear structural interaction problems. The fluid flow is solved by a Particle Finite Element method which is basically fully Lagrangian and the commercial software (ABAQUS) was used for the solid deformation. A domain decomposition method for non-overlapping domains was introduced. The method can handle large deformations of the solid and was applied successfully to the complex fluid-structure interaction problem of a liquid filling an elastic chamber. Yang *et al* [23] extended the Immersed Structural Potential Method (ISPM) of Gil *et al* [15] to include the additional liquid-gas phase boundary by adding a Level Set function. Several benchmark tests were performed to validate their method for two-fluid motion with large solid deformation. The dam break problem with an elastic obstacle was also tested for three-phase interaction.

In this paper, we are aiming at formulating an Eulerian description of deformable solid objects ensuring simple and natural coupling for the fluid and solid interface. An Eulerian transport equation for the solid strain has been implemented with a simple incompressibility constraint to prevent excessive dissipation of the solid strain. Treatment of the solid in an Eulerian fashion can provide valuable advantages since such an approach can be effectively

combined with the fluid solver through matching of the underlying grids. Thus, inclusion of various numerical formulations for additional physics such as interfacial forces due to surface tension, contact modeling, etc. can be straightforward. Most previous work in this area is confined to studies where surface tension effects are less important. In the research presented here, we focus on an Eulerian based formulation for both liquid-gas and fluid-solid interface tracking in the simulation framework of an Eulerian grid for the transport equations with Lagrangian tracking for the interfaces. Special attention is paid to cases where surface tension as well as contact line motion play an important role. In the Eulerian formulation for solid deformation, the method of Sugiyama *et al* [19] is used. Special conditions are also provided to prevent the dissipative loss of stress arising from Eulerian stress advection. Several benchmark tests are performed for droplets impacting on thin flexible membranes in order to demonstrate and investigate this complex three-phase interaction with contact dynamics. Most of our tests are performed for two-dimensional geometries, since our primary objective in this work is to ascertain the applicability of the method for complex three-phase FSI problems. To verify that this approach extends to three-dimensional geometries, we demonstrate a quantitative test of three-phase FSI interaction. In this current paper we first discuss the general description of our interface tracking method, the Level Contour Reconstruction Method (LCRM). Then the Eulerian based numerical scheme including both fluid and solid motion is described. A detailed description for handling solid deformation in the Eulerian frame is presented. Various benchmark tests to investigate the accuracy of this formulation are provided. Finally, the complex three-phase interaction problem of a droplet impacting a flexible cantilever is demonstrated.

2. NUMERICAL FORMULATION

2.1 Interface tracking method

To track the evolving and deforming interfaces for both liquid-gas and fluid-solid, the Level Contour Reconstruction Method (LCRM) will be used[24]. The LCRM takes advantage of concepts from both the Lagrangian Front Tracking and the Eulerian Level Set methods and thus constitutes a hybrid of the two approaches. Separately, the classic Front Tracking[4] and Level Set[2,3] methods have each seen success in applications to various problems in two-phase flow physics and engineering. However, both of the original methods have their drawbacks such as computational complexity for 3D problems in the case of Front Tracking and maintaining mass conservation in the case of the Level Set method. In LCRM, the interface movement is tracked by Lagrangian interface elements which are 1D line segments in 2D formulations or 2D triangular elements for 3D. In this respect the LCRM retains the advantages for interface advection of the original Front Tracking method. Volume conservation in the LCRM is comparable to conventional Front Tracking[4] or Volume of Fluid[1] methods due to the Lagrangian interface tracking characteristics in the LCRM. A detailed study regarding volume conservation can be found in Shin and Juric[26]. However, in our LCRM, the interface elements are implicitly connected, i.e. there is no need for logical connectivity information between neighboring elements which can be quite cumbersome for a 2D mesh of triangular elements in 3D problems. As the interface is advected, its elements need to be regularized from time to time in order to avoid their distortion into overly large or small elements over time.

Here is where the LCRM departs from the original Front Tracking approach and combines aspects of the Level Set method. The LCRM makes use of a Level Set distance function during the operation of interface element regularization. The elements are

regenerated from time to time by reconstructing the elements on the zero contour line of the distance function which is computed directly from the Lagrangian interface throughout the computation (see Fig. 1 for a general schematic). Higher fidelity reconstructed interfaces can be obtained using a high order reconstruction technique[25]. The LCRM method, with such a hybrid of Front Tracking and Level Set characteristics, enables simulations of general and challenging 3D multiphase flows which exhibit arbitrarily large deformations, coalescence and rupture. Several subsequent improvements to the LCRM have been developed in order to essentially eliminate spurious currents (hybrid and compact curvature formulations) even in cases where capillary forces are significant[26,27]. A fully parallelized implementation in a three-dimensional code for high performance computing on massively parallel architectures is detailed in Shin *et al* [28]. The performance of the numerical technique has been benchmarked through various studies[24-29]. Additional features capturing complex interfacial motion have been included in the LCRM including contact line dynamics with contact angle hysteresis and the Fictitious Domain Method for ease of generation of complex solid geometries immersed in the multiphase flow. More details on these extensions can be found in references[24-29].

2.2 Governing equations for the Eulerian based formulation

The governing equations for deformable solid objects interacting with multiphase flows is described in an Eulerian form and here we present the Eulerian based formulation used in this study:

$$\nabla \cdot \mathbf{u} = 0 \tag{1}$$

$$\rho\left(\frac{\partial \mathbf{u}}{\partial t} + \mathbf{u} \cdot \nabla \mathbf{u}\right) = -\nabla p + \rho \mathbf{g} + \nabla \cdot \tilde{\boldsymbol{\sigma}} + \mathbf{f_s} \tag{2}$$

Here **u** is the velocity, *P,* the pressure and **g**, the gravitational acceleration. $\mathbf{f_s}$ is the surface tension force for the liquid-gas interface which will be explained in detail in the next section. The total stress, $\tilde{\boldsymbol{\sigma}}$, represents both the fluid viscous stresses ($\tilde{\boldsymbol{\sigma}}_f$) and those due to solid deformation ($\tilde{\boldsymbol{\sigma}}_s$). The total stress can be described as follows:

$$\tilde{\boldsymbol{\sigma}} = \tilde{\boldsymbol{\sigma}}_f + \tilde{\boldsymbol{\sigma}}_s = \left(1 - H_s\right)\mu_f\left(\nabla\mathbf{u} + \nabla\mathbf{u}^T\right) + H_s\left[\mu_s\left(\nabla\mathbf{u} + \nabla\mathbf{u}^T\right) + \tilde{\boldsymbol{\sigma}}_{sh}\right] \tag{3}$$

Here, $H_s(\phi_s)$ denotes a Heaviside function whose value is zero in the fluid phase and one in the solid phase depending on the solid distance function (ϕ_s) as defined in Eq. (11) below. Here, we include the viscosity of the solid following the formulation of Sugiyama *et al* [17]. For the test cases in this study, the stress from solid deformation ($\tilde{\boldsymbol{\sigma}}_{sh}$) is much higher than that due to viscosity of the solid inside the solid object. For simplicity, we assign the same values of viscosity for the liquid and solid. The stress tensor ($\tilde{\boldsymbol{\sigma}}_{sh}$) can be defined using the left Cauchy-Green strain tensor (**B**) for a Neo-Hookean material as

$$\tilde{\boldsymbol{\sigma}}_{sh} = G\mathbf{B} \tag{4}$$

where G is the shear modulus.

The left Cauchy-Green strain tensor **B** is defined by the deformation tensor (**F**)

$$\mathbf{B} = \mathbf{F}\cdot\mathbf{F}^T \tag{5}$$

For simplicity and without loss of generality we focus on the 2D formulation so that we

can write the deformation tensor, **F,** as

$$\mathbf{F} = \begin{pmatrix} \frac{\partial x}{\partial X} & \frac{\partial x}{\partial Y} \\ \frac{\partial y}{\partial X} & \frac{\partial y}{\partial Y} \end{pmatrix} \tag{6}$$

where (x,y) is the current and (X,Y) is the reference or original location of the material. The 3D formulation is straightforward and key elements are provided in the appendix. Most Finite Element Methods evaluate the deformation tensor field, **F,** directly by tracking Lagrangian element motion.

In this study, we evaluate the left Cauchy-Green strain tensor field directly without computing the deformation tensor field, **B**, using the transport equation provided by Sugiyama *et al* [17]. First, we define a modified left Cauchy-Green strain tensor, **C**, instead of **B** in the same way as Sugiyama *et al* [17] for numerical stability as:

$$\mathbf{C} = H_s^{0.5}\mathbf{B} \tag{7}$$

The transport equation for the modified left Cauchy-Green strain tensor is time advanced according to:

$$\frac{\partial \mathbf{C}}{\partial t} + \mathbf{u}\cdot\nabla\mathbf{C} = \nabla\mathbf{u}^T\cdot\mathbf{C} + \mathbf{C}\cdot\nabla\mathbf{u} \tag{8}$$

In this way, the stress field is confined to the solid region and provides a smoother transition from solid to fluid in order to prevent sudden changes in the stress evolution.

Using Eqs. (4) and (7), Eq. (3) is now:

$$\tilde{\boldsymbol{\sigma}} == \left[\mu_f + (\mu_s - \mu_f)H_s\right]\left(\nabla\mathbf{u} + \nabla\mathbf{u}^T\right) + H_s\tilde{\boldsymbol{\sigma}}_{sh} = \mu\left(\nabla\mathbf{u} + \nabla\mathbf{u}^T\right) + GH_s^{0.5}\mathbf{C} \tag{9}$$

The material property fields can be described using two Heaviside functions as follows:

$$\begin{aligned} b &= (1 - H_s)b_f + H_s b_s \\ b_f &= (1 - H_f)b_l + H_f b_g \end{aligned} \tag{10}$$

where, b represents density or viscosity fields with the subscripts *s, f, l, g* standing for solid, fluid, liquid or gas, respectively. The two Heaviside functions, H_s and H_f, can be computed from the two distance functions distinguishing the fluid-solid (ϕ_s) or the liquid-gas (ϕ_f) respectively.

$$\begin{cases} H_s(\phi_s) = 1, & \phi_s \geq 0 \\ H_s(\phi_s) = 0, & \phi_s < 0 \end{cases} \qquad \begin{cases} H_f(\phi_f) = 1, & \phi_f \geq 0 \\ H_f(\phi_f) = 0, & \phi_f < 0 \end{cases} \tag{11}$$

2.3 Solution procedure

The detailed method for solving the Navier-Stokes equations for the fluid can be found in references[24-28]. Here we briefly describe the basic procedure for the fluid and then focus on the solution for solid deformation. We solve the fluid flow and solid motion separately. For the fluid, the standard incompressible Navier-Stokes equations are:

$$\nabla \cdot \mathbf{u}_f = 0 \tag{12}$$

$$\rho\left(\frac{\partial \mathbf{u}_f}{\partial t}+\mathbf{u}_f\cdot\nabla\mathbf{u}_f\right)=-\nabla p+\rho\mathbf{g}+\nabla\cdot\left\{\mu\left(\nabla\mathbf{u}_f+\nabla\mathbf{u}_f{}^T\right)\right\}+\mathbf{f_s} \qquad (13)$$

where $\mathbf{u}_f$ is the fluid velocity. For the solid deformation, an additional stress field is included.

$$\nabla\cdot\mathbf{u}_s=0 \qquad (14)$$

$$\rho\left(\frac{\partial \mathbf{u}_s}{\partial t}+\mathbf{u}_s\cdot\nabla\mathbf{u}_s\right)=-\nabla p+\rho\mathbf{g}+\nabla\cdot\left\{\mu\left(\nabla\mathbf{u}_s+\nabla\mathbf{u}_s{}^T\right)+\tilde{\boldsymbol{\sigma}}'_{sh}\right\}+\mathbf{f_s} \qquad (15)$$

here, $\tilde{\boldsymbol{\sigma}}'_{sh}$ is the last term on the right side of Eq. (9) and $\mathbf{u}_s$ is the solid velocity field. The solution for solid deformation follows a similar procedure to that for fluid motion. The solid velocity field can be considered as an additional auxiliary field used to advance the solid motion in time in the Eulerian frame (i.e. updated using Eq. (23)). The coupling of the velocity between fluid and solid is forced by matching the boundary condition for the fluid velocity to the solid motion:

$$\mathbf{u}_f=\mathbf{u}_s \quad (\phi_s\geq 0) \qquad (16)$$

The velocities inside the solid ($\phi_s > 0$) are used to update the fluid velocities. The pressure will be solved separately for Eqs. (13) and (15) to enforce the divergence free condition (see Eq. 34). Thus we are basically solving the same Navier-Stokes equations (13) and (15) twice which adds to the computational cost. The only difference between the solution of $\mathbf{u}_f$ and $\mathbf{u}_s$ is near the solid interface. The justification for this choice of separate computation for the fluid and the solid motion is that when only a single velocity field is computed for the entire domain (i.e. $\mathbf{u}_s$) we observe that the smooth transition of the solid

stress at the fluid-solid boundary in the Eulerian description of the stress field can cause the appearance of an artificially high viscous fluid layer adjacent to the solid. This high viscosity fluid layer interferes with the motion of the liquid-gas interface in this region thus inhibiting the wetting behavior of the liquid-gas interface on the solid wall. With a separate computation of the solid velocity and stress field this artificial layer is avoided. The sharp transition of the fluid velocity near the solid object using Eq. (16) makes the phase interface of the fluid interact more smoothly with the solid surface.

This smooth interaction between the fluid and solid interface is necessary for proper treatment of the contact line motion. We account for contact line hysteresis using constant advancing (θ_a) and receding (θ_r) contact angles. Implementation of the contact line dynamics is very straightforward since we are tracking the actual interface element motion with the LCRM. In this study, we used a simple Navier-Slip model. The contact line velocity can be found via :

$$U_{cl} = \lambda \left. \frac{\partial u}{\partial n} \right|_{wall} \tag{17}$$

Here, U_{cl} is the contact line speed, $\partial u/\partial n|_{\text{wall}}$ is the shear strain rate at the wall, and λ is a proportionality slip constant which has been assigned to the size of a grid cell in this study. The interface contact angle is adjusted to match the hysteresis condition. If the apparent contact angle which is the angle between the fluid interface and the the solid interface at the contact line is greater than the advancing angle or less than the receding angle then the contact angle is fixed to either the advancing or the receding angle, respectively. Otherwise, the contact angle is free to move between the advancing and receding angle. A more detailed discussion of the contact line treatment can be found in Shin *et al*[29]

A hybrid formulation for the surface tension force term, $\mathbf{f_s}$, is used to minimize parasitic currents:

$$\mathbf{f_s} = \gamma \kappa_H \nabla H_f\left(\phi_f\right) \tag{18}$$

Here γ represents the surface tension coefficient which is assumed to be constant in our current study and κ_H is the hybrid curvature. The term $\gamma\kappa_H$ can be computed as follows[26, 27]:

$$\gamma \kappa_H = \frac{\mathbf{f}_{\mathbf{s}\mathrm{L}} \cdot \mathbf{G}}{\mathbf{G} \cdot \mathbf{G}} \tag{19}$$

where

$$\mathbf{f}_{\mathbf{s}\mathrm{L}} = \int \gamma \kappa_f \mathbf{n}_f \delta(\mathbf{x} - \mathbf{x}_f) dA \tag{20}$$

$$\mathbf{G} = \int \mathbf{n}_f \delta(\mathbf{x} - \mathbf{x}_f) dA \tag{21}$$

here $\mathbf{x}_f$ is a parameterization of the interface and the geometric information, interface curvature, κ_f, unit normal, $\mathbf{n}_f$, and area of the interface element, dA are computed directly from the Lagrangian interface. $\delta(\mathbf{x}\text{-}\mathbf{x}_f)$ is the delta function that is non-zero only at the interface.

The interfacial elements for the liquid-gas and fluid-solid interfaces are advected in a Lagrangian fashion by integrating, respectively:

$$\frac{d\mathbf{X}_f}{dt} = \mathbf{V}_f \tag{22}$$

$$\frac{d\mathbf{X}_s}{dt} = \mathbf{V}_s \tag{23}$$

with a second order Runge-Kutta method where both interface velocities, $\mathbf{V}_f$ and $\mathbf{V}_s$, are interpolated from the Eulerian field. A detailed description of the interface method as well as the overall numerical procedure for the fluid solution can be found in references[24-27].

Here we focus on the solution procedure for the solid deformation. Basically, the solution procedure for the solid motion (Eqs. (14) and (15)) is similar to that for the fluid motion. The main difference is the inclusion of the left Cauchy-Green strain tensor. The governing equation for the solid is solved using a conventional projection method on a staggered grid[30,31]. The pressure, property fields and distance function are located at the cell centers of the Cartesian mesh while velocity components are located at the cell faces as in Fig. 2. For the stress field, we place the diagonal components (B_{xx}, B_{yy}) at cell centers and the off-diagonal component (B_{xy}) at cell vertices following the work of Sugiyama *et al* [17] (see Fig. 2). Again, we point out that we will focus on the 2D formulation for simplicity. The grid structure in 3D can be found in the appendix. Grouping the advection, viscous diffusion, left Cauchy-Green strain, and gravitational terms into **A**, the discrete form of Eq. (15) can be written as follows:

$$\frac{\mathbf{u}_s^{n+1} - \mathbf{u}_s^n}{\Delta t} = \frac{1}{\rho^n}\left(\mathbf{A}^n + \mathbf{f}_s{}^n\right) - \frac{1}{\rho^n}\nabla_h P \tag{24}$$

here the subscript *h* implies a spatially discrete operator. The convection term is discretized with a second order ENO method[32] and central differences are used for the diffusion term. The 2D transport equation for the left Cauchy-Green strain can be written as follows:

$$\begin{aligned}
&\frac{\partial B_{xx}}{\partial t}+u_s\frac{\partial B_{xx}}{\partial x}+v_s\frac{\partial B_{xx}}{\partial y}=2\left\{\frac{\partial u_s}{\partial x}B_{xx}+\frac{\partial u_s}{\partial y}B_{xy}\right\}\\
&\frac{\partial B_{xy}}{\partial t}+u_s\frac{\partial B_{xy}}{\partial x}+v_s\frac{\partial B_{xy}}{\partial y}=\frac{\partial v_s}{\partial x}B_{xx}+\frac{\partial u_s}{\partial y}B_{yy}\\
&\frac{\partial B_{yy}}{\partial t}+u_s\frac{\partial B_{yy}}{\partial x}+v_s\frac{\partial B_{yy}}{\partial y}=2\left\{\frac{\partial v_s}{\partial x}B_{xy}+\frac{\partial v_s}{\partial y}B_{yy}\right\}
\end{aligned} \tag{25}$$

Here, the right-hand side term can be computed using conventional centered differences (the full 3D formulation for the strain transport can be found in the appendix). Since the strain field transport is computed in the Eulerian frame and since the convective nature is dominant, the strain field could become strongly dissipative unless an appropriate advection scheme for the convective terms is used. In the work of Sugiyama *et al* [17], 5th order advection schemes are utilized to prevent high dissipation of the strain field. Considering the Lagrangian nature of the solid motion we instead use a semi-Lagrangian method[33] for the convective terms on the left-hand side of Eq. (25).

In our current study, the method is formulated to avoid strain dissipation by ensuring the incompressibility constraint. For an incompressible, hyper-elastic material, the strain field should satisfy the following constraint, i.e. unity of the determinant of the left Cauchy strain tensor:

$$\det(\mathbf{B}) = B_{xx}B_{yy} - B_{xy}^2 = 1 \tag{26}$$

Since we are using a modified (filtered) strain field, **C**, the above equation can be cast into:

$$\det(\mathbf{C}) = C_{xx}C_{yy} - C_{xy}^2 = H_s \tag{27}$$

During the simulation, we calculate the left-hand side of Eq. (27) to find an H_c :

$$C_{xx}C_{yy} - C_{xy}^2 = H_c \tag{28}$$

which is not, in general, equal to H_s. In order to ensure that H_c will be the same as H_s, we modify the **C** field by dividing by $\sqrt{H_s / H_c}$. This technique for numerically enforcing the incompressibility constraint was used by Zhao *et al* [10]. The formulation for 3D geometry can be found in the appendix. The above strain transport equation, Eq. (25), is integrated using a 2nd order semi-Lagrangian method[33] with initial strain free field as $\left[H_s(\phi_s)\right]^{0.5}\mathbf{I}$, where **I** represents the identity matrix.

We implement semi-Lagrangian advection by considering the left-hand sides of Eq. (25) in a Lagrangian way. For example, the B_{xx} term can be integrated in time as follows:

$$\frac{\partial B_{xx}}{\partial t} + u_s \frac{\partial B_{xx}}{\partial x} + v_s \frac{\partial B_{xx}}{\partial y} = \frac{dB_{xx}}{dt} = \frac{{B_{xx}}^{n+1} - {B_{xx@d}}^{n}}{\Delta t} = 2\left\{ \frac{\partial u_s}{\partial x} B_{xx} + \frac{\partial u_s}{\partial y} B_{xy} \right\}^n \tag{29}$$

$$\frac{d\mathbf{x}}{dt} = \mathbf{u}_s(\mathbf{x}, t), \qquad \mathbf{x}^{n+1} = \mathbf{x}\left(t^{n+1}\right) = \mathbf{x}_a \tag{30}$$

here, $B_{xx@d}$ represents the strain component B_{xx} at the departure location. The subscript, a, denotes the arrival location of the advected quantity, which, in the semi-Lagrangian method, is defined to coincide with the location of the grid node, $\mathbf{x}^{n+1}$, at which the strain component

at time n+1, B_{xx}^{n+1} is to be calculated. Thus, the departure location, $\mathbf{x}_d$, can be computed from the initial location $\mathbf{x}^{n+1}=\mathbf{x}_a$ using backward differences in time:

$$\hat{\mathbf{x}} = \mathbf{x}_a - \frac{\Delta t}{2}\mathbf{u}(\mathbf{x}_a, t^n) \tag{31}$$

$$\mathbf{x}_d = \mathbf{x}_a - \Delta t \mathbf{u}(\hat{\mathbf{x}}, t^n + \frac{\Delta t}{2}) \tag{32}$$

Knowing the arrival location point ($\mathbf{x}_a$), we find an intermediate point ($\hat{\mathbf{x}}$) using Eq. (31). Then the departure location ($\mathbf{x}_d$) can be obtained using Eq. (32) with velocity interpolated at the intermediate point $\hat{\mathbf{x}}$. The explicit form of the semi-Lagrangian method was used. We did not find significant improvement using the implicit form which requires additional iterations.

Time integration of Eq. (24) was performed in two sub-steps:

$$\frac{\tilde{\mathbf{u}}_s - \mathbf{u}_s^n}{\Delta t} = \frac{1}{\rho^n}\left(\mathbf{A}^n + \mathbf{f}_s{}^n\right) \tag{33}$$

and

$$\frac{\mathbf{u}_s^{n+1} - \tilde{\mathbf{u}}_s}{\Delta t} = -\frac{1}{\rho^n}\nabla_h P \tag{34}$$

here the variable $\tilde{\mathbf{u}}_s$ is the new velocity while ignoring pressure. By enforcing $\mathbf{u}_s^{n+1}$ to be divergence free, the pressure can be found by solving

$$\nabla_h \cdot \left(\frac{1}{\rho^n}\nabla_h P\right) = \frac{\nabla_h \cdot \tilde{\mathbf{u}}_s}{\Delta t} \tag{35}$$

The updated velocity is

$$\mathbf{u}_s^{n+1} = \tilde{\mathbf{u}}_s - \frac{\Delta t}{\rho^n} \nabla_h P \tag{36}$$

Since this numerical approach for the solid velocity is exactly the same as that for the fluid flow[24-27], the solution procedure for the solid motion is identical to the fluid movement except for the inclusion of the stress field.

Recently, our interface tracking method, i.e. Level Contour Reconstruction Method, has been extended to fully three-dimensional simulations using a high-performance code on large-scale parallel computing architectures[28]. The method can handle large property differences, where density and viscosity ratios are on the order of several thousand. Owing to the Level Set characteristics of the LCRM, parallelization is relatively straightforward. The program is built on a modular basis thus application of the code to a wide variety of physical scenarios is possible. Detailed parallel performance characteristics of the code can be found in reference[28]. However, in this work we mainly use a planar 2D formulation for various benchmark tests. As described above, extension to 3D is straightforward since the solid motion can be treated identically to the fluid except for the addition of the left Cauchy-Green strain term in Eq. (15) which is coupled to the solution for strain transport (Eq. (25)). The key elements for the 3D formulation including the grid structure, equation for the strain transport, and incompressibility constraint can be found in the appendix. We have implemented the full three-dimensional strain transport formulation and we provide qualitative results for several relatively simple test cases to demonstrate the applicability of the method in 3D.

3. RESULTS AND DISCUSSIONS

3.1 Benchmark tests

In this section we describe several benchmark tests which we have performed to verify the accuracy of the formulation for deformable solids described in the previous section. Our benchmark tests focus on 2D geometries primarily for ease of quantitative comparisons with existing data. Since our procedures for the problem of interface motion in liquid-gas, i.e. fluid-fluid, systems have already been tested and validated in various applications[24-29], we focus on the FSI problem of the motion of a deformable solid interacting with a fluid.

First, we simulate the behavior of a hyper-elastic material in time varying shear flow. The simulation geometry is shown in Fig. 3. The size of the simulation domain is 2 *m* by 2 *m*. Initially a neo-Hookean solid (shear modulus G=0.2 *Pa*) of thickness 0.5 *m* is placed horizontally at the bottom of the simulation domain. Both the density and viscosity of the liquid and solid are set to 1 kg/m^3 and 0.2 $N{\cdot}s/m^2$, respectively. Periodic boundary conditions are applied at the left and right boundaries and a no-slip, zero velocity condition is applied at the bottom boundary. The top boundary is prescribed a time varying horizontal velocity (in *m/s*) as follows:

$$U(x)=\begin{cases} 0.5\sin^2(\pi x/0.6) & 0\le x\le 3 \\ 1 & 0.3\le x\le 1.7 \\ \sin(\pi(x-2)/0.6) & 1.7\le x\le 2.0 \end{cases} \tag{37}$$

Our simulation results are compared with an existing solution from Zhao *et al* [10]. As can be seen in Fig. 4(a), the current result with a grid resolution of 200×200 matches well with their existing solution. We also performed a grid convergence test (see Fig. 4(b)). The L_2

norm defined by Eq. (38) is plotted for different grid resolutions.

$$L_2\ norm = \frac{\sqrt{\sum_{i=1}^{N}\left(y_c - y_e\right)_i^2}}{N} \tag{38}$$

Here, y_c represents the vertical position of the computed interface location corresponding to a reference location (i.e. y_e) from the existing data of Zhao *et al* [10]. N is the number of data points used in the comparison. Our result demonstrates between 1st and 2nd order accuracy which is comparable to the existing solution[10].

As a second test, we simulate the movement of a deformable solid in a lid-driven cavity flow. The domain size is 1 *m* by 1 *m* and the upper wall moves with a constant velocity of 1 *m*/*s* as can be seen in Fig. 5. No-slip wall conditions are placed at the remaining boundaries. Initially, a cylindrical solid object with radius of 0.2 *m* is placed at (x_c = 0.6 *m*, y_c = 0.5 *m*) in the simulation domain. Both the density and viscosity of the fluid and solid are 1 kg/m^3 and 0.01 $N{\cdot}s/m^2$, respectively. A neo-Hookean material with shear modulus G=0.1 *Pa* is used as the deformable solid. The centroid of the deformable solid is traced in time (see Fig. 6(a)). As can be seen from the figure, our result shows grid convergent behavior and good comparison with existing data even with quite low resolution. The convergence rate was computed in Fig. 6(b) using the L_2 norm. The distance between the computed position of the solid centroid and reference position from Sugiyama *et al* [17] is compared. The convergence rate shows between 1st and 2nd order accuracy. More detailed snapshots in time of the interfacial shapes for the solid are plotted in Fig. 7. The interface shapes at different times are compared to the highest resolution results from Sugiyama *et al* [17]. The interface shapes from our current simulation for a 400×400 grid are nearly comparable to the highest resolution results of Sugiyama *et al* [17] for their 1024×1024 grid.

A third benchmark test is for a vibrating flat plate attached to a blunt object (cylinder) in Poiseuille flow. The detailed simulation geometry is shown in Fig. 8(a). A parabolic velocity profile with U as 2 m/s is prescribed at the left boundary as shown in the figure. An outflow condition ($\partial u/\partial x = \partial v/\partial x = 0$) is placed at the right boundary and a no-slip wall condition is used at the top and bottom boundaries. Neumann conditions for pressure have been applied for all boundaries. The size of the simulation domain is 1.64 m × 0.41 m with a grid resolution of 400×100. A cylindrical stationary object is located at (0.2 m, 0.2 m) with a diameter of D = 0.1 m. The Reynolds number with respect to cylindrical object ($Re = \rho UD/\mu$) is 200. A thin flexible plate of length 0.35 m and thickness 0.02 m is attached at the downstream face of the cylinder. Both the density and viscosity of the fluid and solid are 1000 kg/m^3 and 1 $N{\cdot}s/m^2$, respectively. For the deformable solid, a neo-Hookean material with shear modulus of G= 2×10^6 Pa is used. A snapshot of the deformed solid with velocity magnitude contours is shown in Fig. 8(b). Under these flow conditions, the cylindrical object sheds downstream vortices which act to bend the flexible plate, which fluctuates vertically with time due to the regular passage of fluid vortices. One can clearly see the vortex shedding behind the cylinder resulting in deflection of the deformable solid plate. We trace the motion of the right-hand tip of the membrane with time in Fig. 9. At first, the amplitude of the vertical tip location fluctuation increases with time after which the fluctuation amplitude and frequency show a regular rhythmic oscillation in time. This result is compared with the existing solution of Turek and Hron[34]. The current simulation results match very well with their existing solution.

Our final benchmark test is more challenging. An initially vertical thin membrane is placed at the bottom center (4 m, 0 m) of an 8 m × 1 m simulation domain (see Fig. 10) of height 0.8 m and thickness 0.0212 m with a grid resolution of 800×100. An oscillating flow (period T=1 s) of $u(y) = 1.5Uy(2\text{-}y)\sin(2\pi/T)$ and $v = 0$ is imposed at the left inlet with an

outlet flow condition ($\partial u/\partial x = \partial v/\partial x = 0$) at the right boundary. Neumann conditions for pressure have been applied for all boundaries. A symmetry condition is used at the top boundary and no-slip condition at the bottom boundary. Both the density and viscosity of the fluid and solid are 1 kg/m^3 and 0.01 $N{\cdot}s/m^2$, respectively. A neo-Hookean material is used for the deformable solid membrane with a shear modulus G=1000 Pa. Under these conditions, the thin membrane will deform severely due to the oscillatory flow. Snapshots of the deformable membrane motion with time are plotted in Fig. 11. The initially upright membrane is first deflected strongly to the right in the initial phase of the inlet flow of fluid. The upper portion of the membrane bends parallel to the flow direction and then, as the flow direction reverses, the membrane also reverses direction in a hook-shaped whipping motion. At non-dimensional time t/T=0.8 the thin membrane again becomes parallel to the flow but now pointing in the opposite direction. Even with such large deformation, our solution method can maintain the narrow width of the membrane throughout the simulation. The interface motion is very similar to other numerical results[6,8,14,15].

3.2 Three-phase interaction – droplet impact on a flexible cantilever in 2D

We test our formulation for the case of a three-phase problem of a liquid droplet impacting a flexible solid cantilever. All three phases, solid, liquid and surrounding gas as well as their complex liquid-gas and fluid-solid interface motions are included in the computation. In this test, particular attention is paid to the effects of surface tension and three-phase contact line motion on the solid. As can be seen in Fig. 12, we consider the case of a cantilever, initially positioned horizontally, as it is impacted by a water droplet falling due to gravity. The simulation domain has a height of 0.08 m and length of 0.04 m with a grid resolution of 200×400. One side of the cantilever is fixed at the left boundary at a height of 0.06 m from the bottom boundary. The length and width of the cantilever are 0.02 m and

0.0008 *m*, respectively. A neo-Hookean material with shear modulus G=4×10^5 *Pa* is used for the solid. The density of the solid material is 1500 *kg/m*^{3}, for the liquid the density is 1000 *kg/m*^{3} and for the gas the density is 1 *kg/m*^{3}. The viscosity of the solid and liquid are both 0.001 *N·s/m*^{2}. The gas viscosity is 0.00001 *N·s/m*^{2}. The liquid-gas surface tension coefficient is set to 0.075 *N/m*. An advancing contact angle (θ_a) of 100^o and receding angle (θ_r) of 80^o are selected (we will denote this angle configuration as the reference case for the contact angle study at the end of section 3.2). The droplet with diameter of 0.012 *m* is initially placed at (*x,y*)= (0.02 *m*, 0.072 *m*).

The first computation we perform is that of natural deflection of the cantilever due to gravity (no droplet). Fig. 13 shows several snapshots of the cantilever with velocity vectors. In the inset to Fig. 13, the movement of the center of the right-side tip of the cantilever is plotted with time. The position of the tip drops down at first but rebounds upward due to the elasticity of the cantilever. The vertical position of the cantilever tip oscillates until reaching a steady position. We also plot velocity vectors near the peak location of the tip position (Fig. 13 (a)-(d)). We can identify a circular vortex near the tip. As the right-side tip bends downward (Fig. 13 (a) and (c)), a counter-clock wise vortex is generated at the top of the cantilever. A clockwise vortex can be observed below the cantilever during upward rebound (Fig. 13 (b) and (d)).

Next, we place a water droplet slightly above the thin cantilever as shown in Fig. 12. The overall interface evolution of this three-phase interaction is shown in Fig. 14. The liquid-gas interface is plotted with a red line and the deformable solid interface in blue. The initially circular liquid-gas interface falls down to the cantilever (already deforming prior to droplet impact due to its own weight). The liquid-gas interface maintains its original circular shape before impact due to its relatively high surface tension. At a time of about 0.05 *s*, the droplet hits and wets the bent solid surface. Due to the sloping angle of the bent cantilever,

the droplet slips to the right. Due to surface tension at the contact region, the droplet elongates with the elongation becoming larger and with one end of the droplet attached to the right tip of the cantilever. Finally, the elongated droplet detaches from the solid surface trailing a liquid thread which breaks up into several satellite droplets.

Before further analyzing the three-phase interaction more closely, we study the grid convergence for this case. Deflections of the central tip at the free end of the cantilever are compared at four different mesh resolutions (see Fig. 15). Due to the severe time restriction at the highest resolution, only the initial deflection stage is compared. As can be seen in the figure, the amount of the tip deflection converges as the mesh size decreases. With a resolution of 200×400, the solution can be considered to be converged. We note that the movement of the cantilever can be quantitatively well captured at all except the lowest 50×100 resolution.

In Fig. 16 we compare the amount of cantilever deflection with droplet impact to the amount of deflection due to gravity alone. With gravity alone (no droplet impact), the solid cantilever oscillates in time to reach a final steady position as already seen in Fig. 13. With droplet impact at the tip of the cantilever the deflection becomes much larger. In Fig. 16, we also include the interaction between the droplet and the thin cantilever when the density of the solid is reduced to 100 kg/m^3. We choose a much lower solid density in order to observe the droplet impact behavior more clearly without natural deflection due to gravity. As can be seen in the figure, the droplet impacts the less dense cantilever slightly earlier in time since the less dense cantilever is deflected less by its own weight. However, once the droplet impacts, the slope of the deflection vs. time curves are very similar for both cases, which indicates that the downward speed of the cantilever tip due to droplet impact is not influenced much by the solid density but is determined by the impact speed of the droplet alone. After droplet impact the less massive cantilever can be seen to oscillate much more rapidly than the

more massive cantilever. This more rapid oscillation is in agreement with the expected higher natural frequency of a lower mass elastic body in free vibration.

To investigate the effect of solid stiffness, three values of the solid shear modulus ($G = 4\times10^5\ Pa$, $2\times10^6\ Pa$, and $1\times10^7\ Pa$) are used while we maintain the solid density equal to 100 kg/m^3. We chose the lower density solid in order to more clearly observe the effect of droplet impact with minimal natural gravitational deflection of the cantilever before impact. The evolution of the liquid-gas and fluid-solid interfaces are shown in Fig. 17 for G = $2\times10^6\ Pa$ and in Fig. 18 for G=$1\times10^7\ Pa$. (the case with G=$4\times10^5\ Pa$ has already been shown in Fig. 14). With increasing shear modulus, the solid cantilever becomes stiffer and thus exhibits less deflection. The overall behavior is similar to that in Fig. 14. However, the droplet slides and detaches from the stiffer, higher shear modulus and thus less-deflected cantilever farther to the right of the domain. The motion of the right tip of the cantilever, i.e. deflection distance, vs solid stiffness is plotted in Fig. 19. With higher shear modulus, the deflection amplitude is very small and the frequency is high. When the shear modulus is $4\times10^5\ Pa$ (lowest), the right tip of the cantilever oscillates with a larger amplitude and lower frequency. We can also notice that the portion of the droplet remaining on top of the cantilever after droplet breakup is quite different. The volume of liquid remaining on the cantilever increases with increased stiffness. The remaining liquid volume fraction after droplet detachment is plotted for varying shear moduli in Fig. 20 (An additional case with G=$6\times10^6\ Pa$ is added for clarity. The remaining volume is very similar to that with G = $1\times10^7\ Pa$). The trend plotted in Fig. 20 shows that the remaining droplet volume increases sharply at lower shear modulus but converges at higher moduli approaching a value for a rigid cantilever.

Lastly, we study the effect of contact angle on the behavior of the impacting droplet. From the case shown in Fig. 12 and the reference contact angle configuration (θ_a=100^o, θ_r=80^o) used above for comparison, we modify the angles to observe the droplet behavior on

hydrophilic (θ_a=60°, θ_r=30°), hydrophobic (θ_a=160°, θ_r=120°), and super-hydrophobic (θ_a=165°, θ_r=160°) surfaces. Super-hydrophic surfaces which can maintain very high contact angles have been observed in natural environments and have drawn much attention recently for possible applications in various engineering fields[35]. The evolution of the right-side tip of the cantilever is shown in Fig. 21. Although the magnitude of deflection is somewhat different, we can see that the behavior of the tip of the cantilever is qualitatively similar for the reference, hydrophilic, and hydrophobic cases. With increasing contact angle, the maximum initial deflection is slightly decreased but the subsequent deflection of the first rebound is increased. This is mainly due to the increased surface tension force at the contact line pulling the droplet back to a more circular shape for higher contact angles. At higher contact angles the droplet tends to slip off of the cantilever more easily and thus less of its vertical momentum is translated into cantilever deflection at initial impact. However, the droplet tends to pull the cantilever upward due to the increased contact angle thus the first rebound deflection distance is larger. Very interesting behavior can be observed for the super-hydrophobic surface. When both the advancing and receding angles are very high, the cantilever can deflect upward during rebound. A more detailed interface plot is shown in Fig. 22 (other interfaces for different contact angles have not been shown since their behavior is very similar to the reference case in Fig. 14). Up to t = 0.09 *s* the tip of the cantilever is deflected downward as expected due to the droplet impact. The droplet then quickly slips and falls off of the super-hydrophobic cantilever surface. Very little of the drop mass remains on the cantilever and thus this allows the cantilever to rebound a greater distance with the tip deflecting upward before subsequently oscillating. In Fig. 21 we can clearly see the qualitative difference in the cantilever deflection dynamics due to the droplet impact on the super-hydrophobic surface.

3.3 Three phase interaction - droplet impact on a flexible cantilever in 3D

Here we extend the above simulation of drop impact on a flexible cantilever to three-dimensional geometry. In this case the grid resolution is 128×128×256. The basic simulation geometry and physical parameters are the same as in the 2D counterpart (see Fig. 12) except that we now place a sphere above a horizontal plate which has a finite width w= 0.01 m as can be seen in Fig. 23(a). The evolution of the liquid-gas interface as well as the solid interface is presented in Fig. 23 for the case with reference contact angle (θ_a=100^o, θ_r=80^o). The overall motion is very similar to the 2D case. The droplet falls from its initial position and impacts the tip of the free end of the cantilever which deflects downward due to the impact. At impact the droplet deforms with the portion of the droplet impacting the cantilever beginning to form the classic form of a droplet splash on a solid surface while the overhanging portion of the droplet is free to continue falling past the cantilever. As the cantilever continues its downward deflection, the droplet elongates and begins to slide off of the cantilever. Continuing its elongation even as the cantilever rebounds upward, the highly stretched droplet drips completely off of the cantilever tip and as it elongates, breaks up, with the formation of several satellite droplets as also observed in the 2D simulation. The left-right symmetry of the evolving droplet is not explicitly enforced but nevertheless observed throughout the simulation.

In our final simulation we increase the contact angles to (θ_a=165^o, θ_r=160^o) to model a super-hydrophobic surface as in the counterpart 2D case in Fig. 22. The interface evolution is shown in Fig. 24. The initial progression of the droplet deformation is similar to the previous 3D case in Fig 23. However, deflection is relatively small compared to the reference surface. As pointed out earlier, a higher contact angle makes the droplet more spherical thus the droplet tends to slip more on the cantilever. Due to the three-dimensional geometry with finite width of the cantilever, the droplet spreads in both the width and tip directions resulting

in a much smaller deflection of the cantilever. The finite and relatively short width of the cantilever induces early break up of droplet at the corners of the cantilever tip edge. In breaking up in this manner a small portion of the drop remains on top of the cantilever while the rest of the drop elongates in two branch ligaments from either side of the cantilever. These ligaments then further breakup forming several satellite droplets as the bulk of the main droplet falls. Again, the left-right symmetry of the evolving droplet is not explicitly enforced but nevertheless observed throughout the simulation.

For the two 3D cases above, we compare the motion of the center of the free end of the cantilever tip with the 2D test case in Fig. 25. For a more proper comparison, we use the results from a relatively low resolution 100×200 2D simulation. (As shown in Fig. 15, the tip motion at this resolution was not much different than that at higher resolutions.) In general, the cantilever tip deflection is somewhat smaller in 3D for both the reference and super-hydrophobic surface cases than it is in 2D. This can be expected since in 3D the spherical droplet has a relatively smaller mass impacting the cantilever compared with a cylindrical droplet in 2D. The time to maximum cantilever deflection is shorter in 3D followed by higher frequency tip oscillations compared with the 2D case. We note that we present the 3D simulations here only as a qualitative demonstration of the capabilities of our LCRM based Eulerian model to capture the main features of the full fluid-structure interaction in a complex two-phase flow.

4. CONCLUSION

We present an Eulerian based formulation for the interaction of two-phase flows with deformable solids in the framework of the Level Contour Reconstruction Method (LCRM). The solid stress tensor field is transported in the Eulerian frame and thus does not require a Lagrangian description for the stress as in conventional FEM methods. In this way, the solid interface motion can be numerically treated with existing interface tracking methods such as our LCRM. Here we simulate Neo-Hookean materials but additional formulations for different hyper-elastic materials are possible. The advantage of computing the stress field in the Eulerian frame is that the numerical formulation is closely compatible with existing fluid flow solvers. To prevent excessive dissipation due to the convective nature of the solid transport equation, a simple incompressibility constraint for the stress field is enforced. The LCRM is used to track both the liquid-gas and the fluid-solid interfaces. The LCRM is a hybrid of Level Set and Front Tracking methods and adopts advantages of both Level Sets (natural topological change) and Front Tracking (volume conserving without smearing) and has been shown to perform well for many multiphase engineering and fluid physics applications.

Several 2D benchmark tests are performed in order to verify the accuracy of the formulation and numerical approaches developed in this article. The first test we present is for a horizontal solid surface placed at the bottom of the simulation domain subject to an overlying fluid flow with prescribed velocity field. In the second test, we track the time evolution of a cylindrical solid in the canonical driven cavity problem. Both of these benchmark tests show good agreement with existing solutions and grid convergence behavior between 1^{st} and 2^{nd} order. For the third test, we simulate fluid flow coupled to the free motion of a thin deformable solid membrane attached to the rear of a stationary solid cylinder.

Due to the generation of alternating vortices in the wake flow behind the blunt cylinder, the attached thin membrane is induced to oscillate vertically. The amplitude and frequency of the oscillating membrane match very well with an existing high-fidelity FEM solution. In the final test we subject an initially vertical thin solid membrane to very large horizontal deflections due to a horizontally pulsating channel flow. The thin membrane deflects and alternatingly whips to align with the current downstream flow direction. The solid membrane motion is in good agreement with an existing solution even at such very large interface deformations.

For the more complex problem of the interaction of two-phase flow with solid deformation, we test the three-phase interaction problem of a droplet impacting a flexible solid cantilever. This problem involves the complex interplay of liquid-gas interface motion, solid deformation, solid-fluid interface motion and surface tension including contact line dynamics. We include full contact angle hysteresis where advancing and receding angles play an important role. The simulations follow the detailed motion of the droplet impact (and subsequent deformation, breakup and fall trajectory) along with the motion of the deformable solid cantilever due to its own weight as well as due to the force of the droplet impact. We observe that as the droplet impacts and breaks up, a portion of it remains on top of the cantilever and that this remaining droplet fraction increases with higher cantilever stiffness. In order to study the effect of contact line dynamics, we test a variety of contact angle configurations corresponding to hydrophilic, hydrophobic, and super-hydrophobic surfaces. A strong influence of surface tension on the cantilever motion is observed especially for the super-hydrophobic surface which shows that, after the initial downward deflection, the cantilever could rebound to reverse its deflection and point upward.

In extending the formulation and numerical method to three-dimensional geometry, we demonstrate several simulations in fully 3D geometries for the case of a droplet impacting a

cantilever. Although the overall behavior of the droplet and cantilever are generally similar in 3D compared with 2D, certain differences in details of the droplet evolution and cantilever motion are described. The 3D simulations performed here serve only as a qualitative demonstration of the capabilities of our LCRM based Eulerian model to capture the main features of the full fluid-structure interaction in a complex two-phase flow. An in-depth analysis and investigation of the detailed physics of droplet dynamics in such a complex three-phase interaction will be the subject of our future work.

ACKNOWLEDGEMENTS

This work is supported by (1) Basic Science Research Program through the National Research Foundation of Korea (NRF) funded by the Ministry of Education (2017R1D1A1B03028518, 2020R1A2C1003822) and (2) by computing time at the Institut du Developpement et des Ressources en Informatique Scientifique (IDRIS) of the Centre National de la Recherche Scientifique (CNRS), coordinated by GENCI (Grand Equipement National de Calcul Intensif) Grant 2019 A0062B06721.

.

REFERENCES

1. C.W. Hirt, B.D. Nichols, Volume of fluid (VOF) method for the dynamics of free boundaries, *J. Comput. Phys.* (1981), 39, 201-225.
2. S. Osher, J.A. Sethian, Fronts propagating with curvature dependent speed: algorithms based on Hamilton-Jacobi formulations, *J. Comput. Phys*. (1988), 79, 12-49.
3. S. Osher, R.P. Fedkiw, Level Set Methods: an overview and some recent results, *J. Comp. Phys.* (2001), 169, 463-502.
4. G. Tryggvason, R. Scardovelli, S. Zaleski, Direct Numerical Simulations of Gas-Liquid Multiphase Flows, Cambridge University Press, Cambridge, England (2011).
5. J. Donea, S. Giuliani, J.P. Halleux, An arbitrary Lagrangian-Eulerian finite element method for transient dynamic fluid-structure interaction, *Comput. Meth. Appl. Mech. Eng.* (1982), 33, 689-723
6. F.P. T. Baaijens, A fictitious domain/mortar element method for fluid-structure interaction, *Int. J. Numer. Mech. Fluids* (2001), 35, 743-761.
7. R. Glowinski, T.W. Pan, T.I. Hesla, D.D. Joseph, J. Periaux, A fictitious domain approach to the direct numerical simulation of incompressible viscous flow past moving rigid bodies: application to particulate flow, *J. Comput. Phys.* (2001), 169, 363-426.
8. Z. Yu, A DLM/FD method for fluid/flexible-body interactions, *J. Comput. Phys*. (2005), 207, 1-27
9. C.S. Peskin, Numerical analysis of blood flow in the heart, *J. Comput. Phys*. (1977), 25, 220-252.
10. H. Zhao, J. B. Freund, R. D. Moser, A fixed-mesh method for incompressible flow-structure systems with finite solid deformations, *J. Comput. Phys*. (2008), 227, 3114-3140.

11. P. He. and R. Qiao., A full-Eulerian solid level set method for simulation of fluid-structure interaction, *Microfluid Nanofluid* (2001), 11, 557-567
12. W. Huang and H.J. Sung, An immersed boundary method for fluid-flexible structure interaction, *Comput. Methods Appl. Mech. Engrg.* (2009), 198, 2650-2661
13. F. Tian, H. Dai, H. Luo, J.F. Doyle, and B. Rousseau, Fluid-structure interaction involving large deformations: 3D simulations and applications to biological systems, *J. Comput. Phys.* (2014), 258, 451-469
14. C. Jiang, J. Yao, Z. Zhang, G. Gao, and G.R. Liu, A sharp-interface immersed smoothed finite element method for interactions between incompressible flow and large deformation solids, *Comput. Methods Appl. Mech. Engrg.* (2018), 340, 24-53.
15. A.J. Gil, A.A. Carreno, J. Bonet, O. Hassan, The immersed structural potential method for haemodynamic applications, *J. Comput. Phys.* (2010), 229, 8613-8641.
16. A.J. Gil, A.A. Carreno, J. Bonet, O. Hassan, An enhanced immersed structural potential method for fluid-structure interaction, *J. Comput. Phys.* (2013), 250, 178-205.
17. K. Sugiyama, S. Ii, S. Takeuchi, S. Takagi, Y. Matsumoto, A full Eulerian finite difference approach for solving fluid-structure coupling problems, *J. Comput. Phys*. (2011), 230, 596-627
18. S. Ii, X. Gong, K. Sugiyama, J. Wu, H. Huang, and S. Takagi, A full Eulerian fluid-membrane coupling method with a smoothed volume-of-fluid approach, *Commun. Comput. Phys*. (2012), 12(2), 544-576
19. S. Ii, K. Sugiyama, S. Takeuchi, S. Takagi, and Y. Matsumoto, An implicit full Eulerian method for the fluid-structure interaction problem, *Int. J. Numer. Meth. Fluids.* (2011), 65, 150-165

20. H. Esmailzadeh and M. Passandideh-Fard, Numerical and experimental analysis of the fluid-structure interaction in presence of a hyperelastic body, *J. Fluids Eng.* (2014), 136, 111107
21. K. Nishiguchk, R. Bale, S. Okazawa, and M. Tsubokura, Full Eulerian deformable solid-fluid interaction scheme based on building-cube method for large-scale parallel computing, *Int. J. Numer Methods Eng.* (2019), 117, 221-248.
22. S. Meduri, M. Cremonesi, U. Perego, O. Bettinotti, A. Kurkchubasche, and V. Oancea, A partitioned fully explicit Lagrangian finite element method for highly nonlinear fluid-structure interaction problems, *Int. J. Numer. Mech. Engng*. (2018), 113, 43-64.
23. L. Yang, A.J. Gil, A.A. Carreno, J. Bonet, Unified one-fluid formulation for incompressible flexible solids and multiphase flows: application to hydrodynamics using the immersed structural potential method (ISPM), *Int. J. Numer. Method in Fluids* (2018), 86(1), 78-106
24. S. Shin, D. Juric, Modeling three-dimensional multiphase flow using a level contour reconstruction method for front tracking without connectivity, *J. Comput. Phys.* (2002), 180, 427-470.
25. S. Shin, D. Juric, High order level contour reconstruction method, *Journal of Mechanical Science and Technology* (2007), 21(2), 311-326.
26. S. Shin, D. Juric, A hybrid interface method for three-dimensional multiphase flows based on front-tracking and level set techniques, *Int. J. Num. Meth. Fluids* (2009), 60, 753-778.
27. S. Shin, S. I. Abdel-Khalik, V. Daru, D. Juric, Accurate representation of surface tension using the level contour reconstruction method, *J. Comput. Phys.* (2005), 203, 493-516.

28. S. Shin, J. Chergui, D. Juric, A solver for massively parallel direct numerical simulation of three-dimensional multiphase flows, *Journal of Mechanical Science and Technology* (2017), 31(4), 1739-1751.
29. S. Shin, J. Chergui, and D. Juric, Direct simulation of multiphase flows with modeling of dynamic interface contact angle, *Theoretical and Computational Fluid Dynamics* (2018), 32(5), 655-687.
30. A.J. Chorin, Numerical solution of the Navier-Stokes equations, *Math. Comput.* (1968), 22, 745-762.
31. F.H. Harlow and J.E. Welch, Numerical calculation of time dependent viscous incompressible flow of fluid with free surface, *Phys. Fluids* (1965), 8, 2182-2189
32. C.W. Shu, S. Osher, Efficient implementation of essentially non-oscillatory shock capturing schemes II, *J. Comput. Phys.* (1989), 83, 32-78
33. D. Xiu and G. E. Karniadakis, A semi-Lagrangian high-order method for Navier-Stokes equations, *J. Comput. Phys*., (2001), 172, 658-684
34. S. Turek, J. Hron, Proposal for numerical benchmarking of fluid-structure interaction between an elastic object and laminar incompressible flow, Fluid-Structure Interaction: Modelling, Simulation, Optimisation, Springer-Verlag, 2006
35. Y. Nam, H. Kim, S. Shin, Energy and hydrodynamic analyses of coalescence-induced jumping droplet, *Appl. Phys. Lett*. (2013), 103, 161601

FIGURE CAPTIONS

Fig. 1 General description of the LCRM.

Fig. 2 Grid structure for the 2D geometry.

Fig. 3 Simulation schematics for the evolution of the horizontal Neo-Hookean material under an imposed velocity of the top wall of the channel.

Fig. 4 Simulation results for the evolution of the horizontal Neo-Hookean material (a) final interface shape compared to the existing data (b) convergence behavior.

Fig. 5 Simulation settings for the cylindrical Neo-Hookean material in a driven cavity.

Fig. 6 (a) Evolution profile for the centroid location of the hyper-elastic material with varying grid resolution (b) convergence behavior.

Fig. 7 Interface shape vs. time for the cylindrical Neo-Hookean material in driven cavity.

Fig. 8 (a) Simulation geometry and settings for the thin flexible membrane attached to the blunt object in Poiseuille flow field (b) Interface shape of the deflecting solid with velocity magnitude contour.

Fig. 9 Comparison of the trace point at the tip of the membrane with existing data for the flexible membrane attached to the circular object.

Fig. 10 Simulation schematics for the vertical flexible membrane under pulsating flow.

Fig. 11 Solid interface evolution vs time for the vertical flexible membrane under pulsating flow.

Fig. 12 Simulation geometry and settings for the three-phase interaction problem (droplet impact on a flexible cantilever).

Fig. 13 Natural deflection of the thin membrane under gravity with velocity vector field (motion of the right tip of the cantilever is shown at the top-right of the figure).

Fig. 14 Interface evolution for the three-phase interaction problem with $G = 4\times10^5\ Pa$.

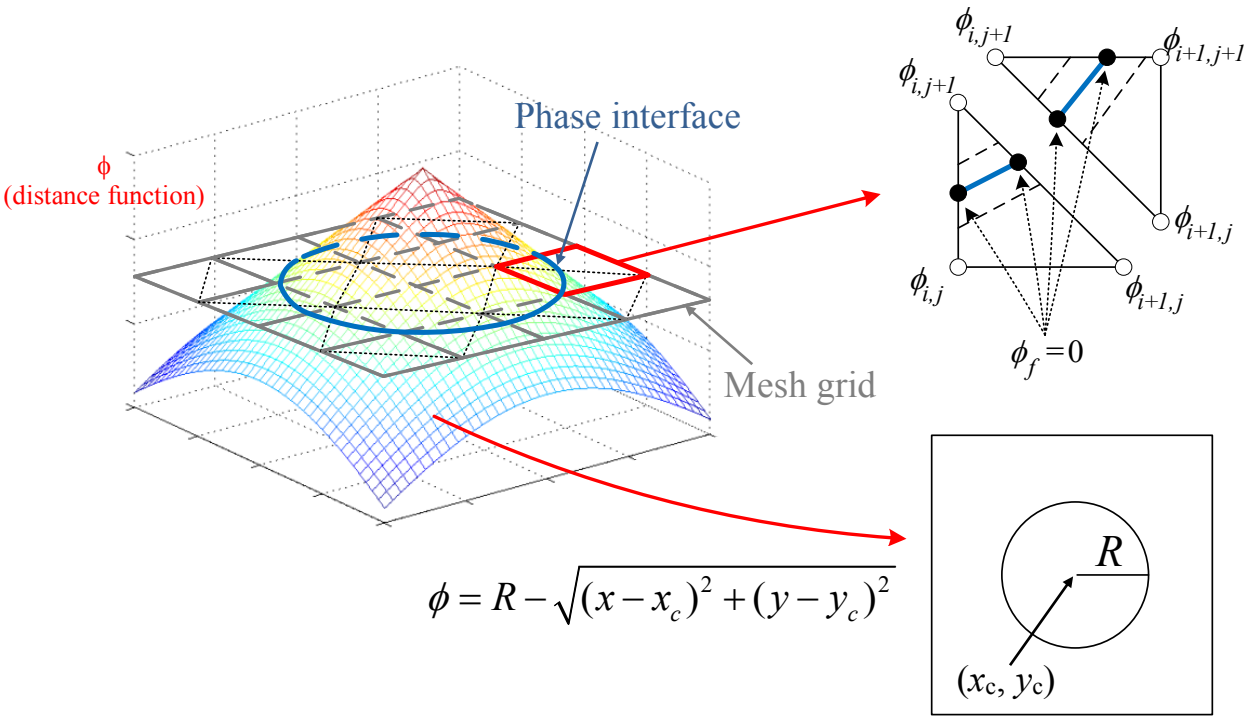
ϕ
(distance function)
Phase interface
Mesh grid
$\phi_{i,j+1}$
$\phi_{i+1,j+1}$
$\phi_{i,j+1}$
$\phi_{i+1,j}$
$\phi_{i,j}$
$\phi_{i+1,j}$
$\phi_f = 0$
$\phi = R - \sqrt{(x-x_c)^2 + (y-y_c)^2}$
R
(x_c, y_c)

Fig. 1

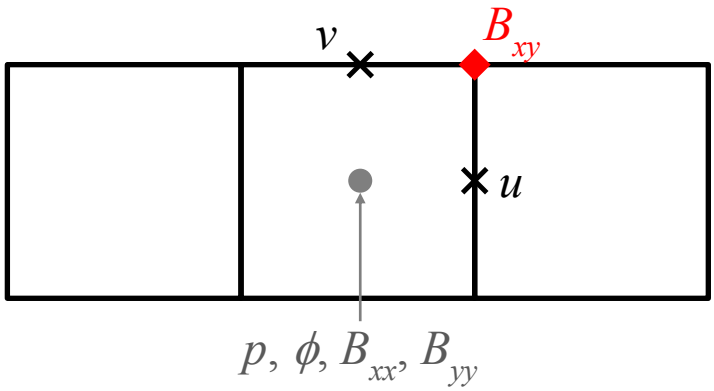

Fig. 2

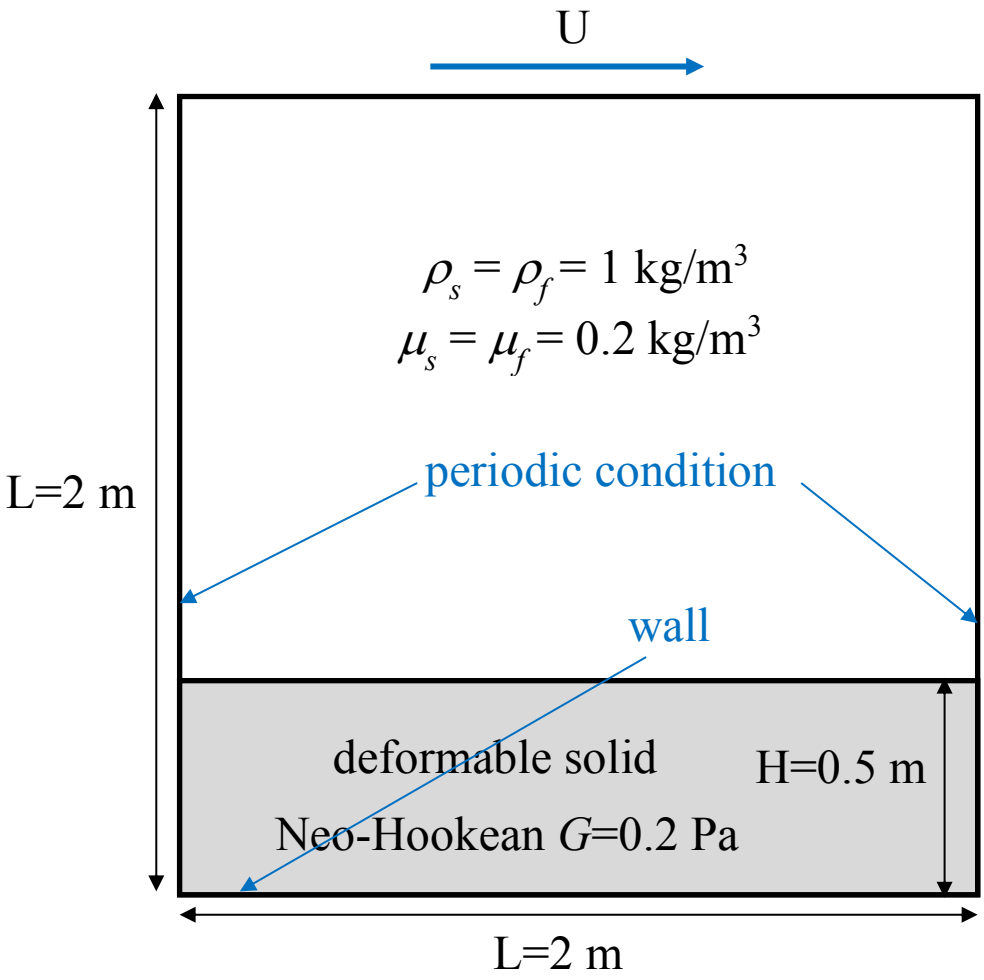
U
$\rho_s = \rho_f = 1$ kg/m^3
$\mu_s = \mu_f = 0.2$ kg/m^3
periodic condition
wall
deformable solid
Neo-Hookean G=0.2 Pa
H=0.5 m
L=2 m
L=2 m

Fig. 3

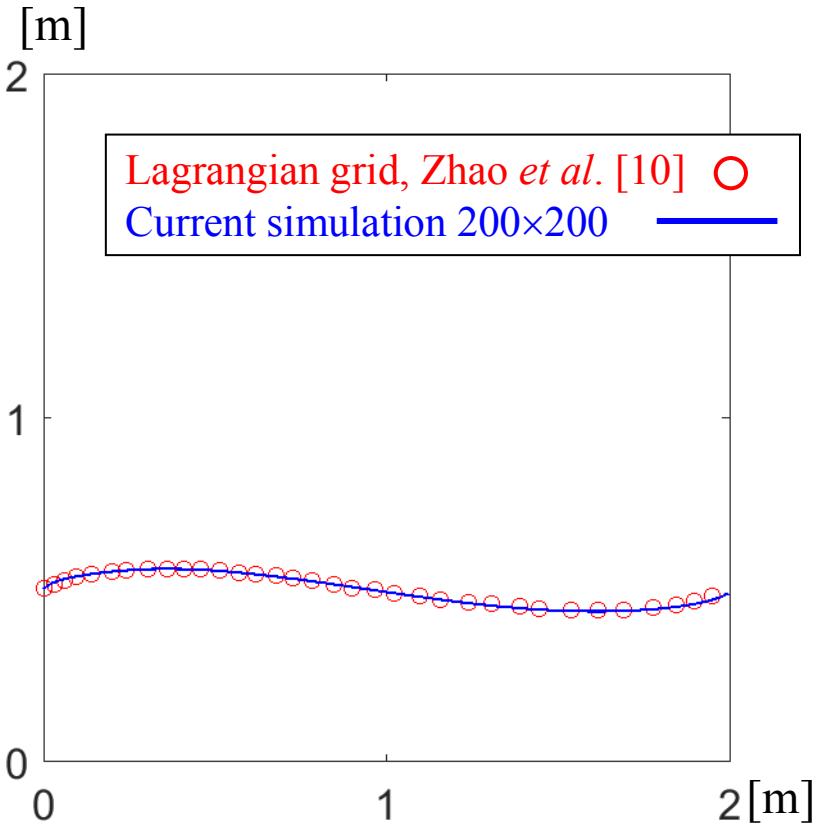
[m]
2
1
0
0
1
2
[m]
Lagrangian grid, Zhao et al. [10]
Current simulation 200×200

(a)

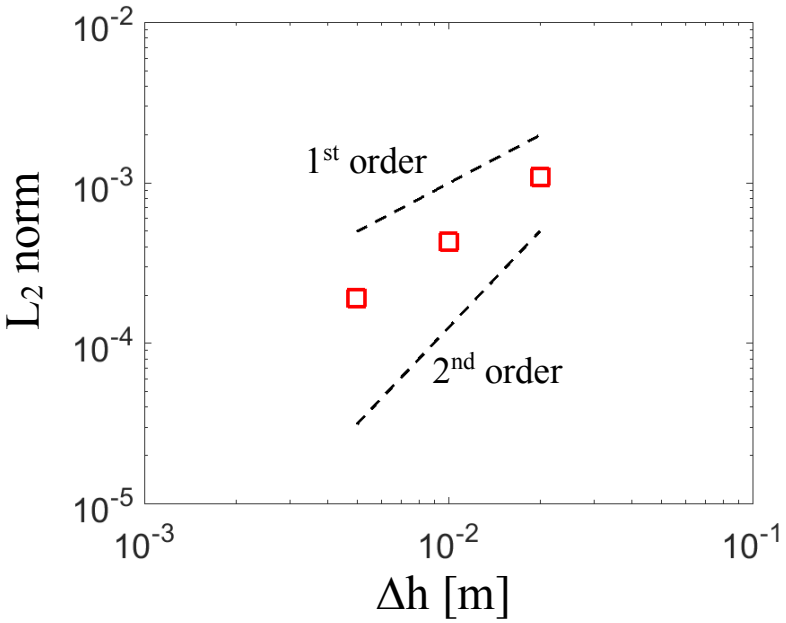
10^{-2}
10^{-3}
10^{-4}
10^{-5}
L_2 norm
1st order
2nd order
10^{-3}
10^{-2}
10^{-1}
Δh [m]

(b)

Fig. 4

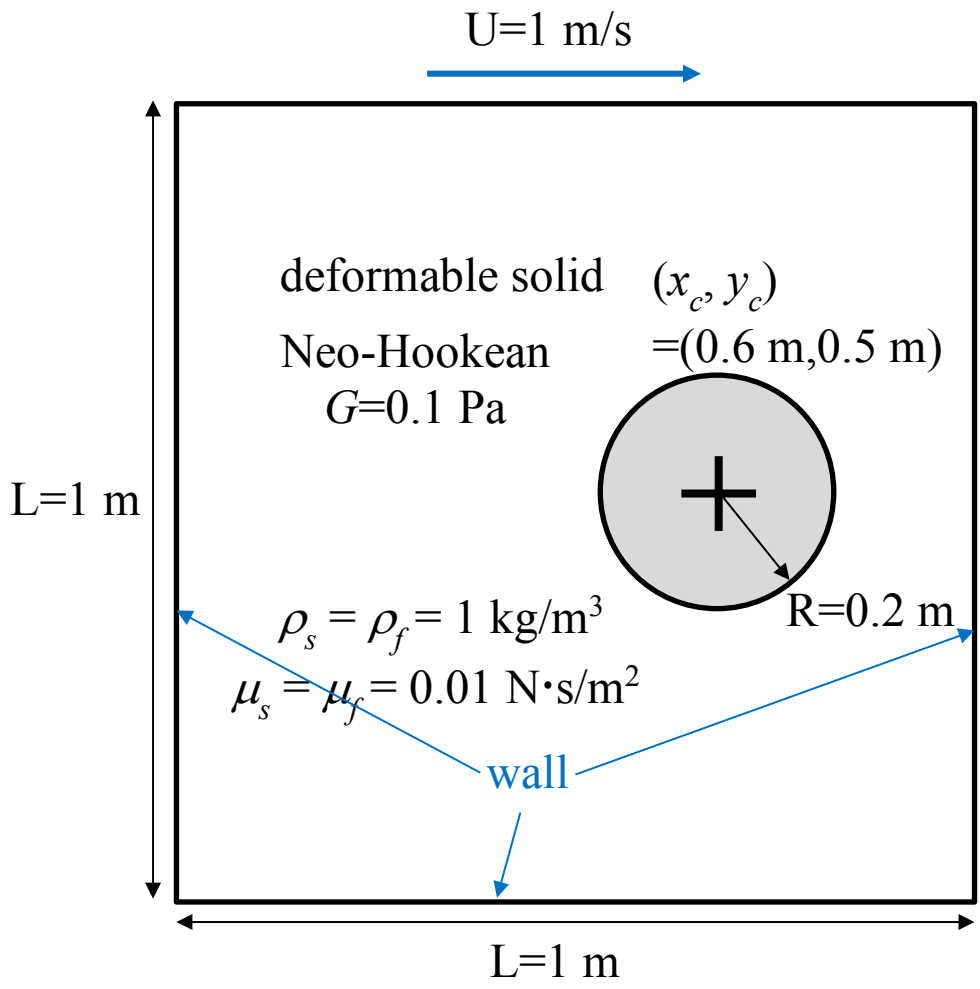
U=1 m/s
deformable solid
Neo-Hookean
G=0.1 Pa
(x_c, y_c)
=(0.6 m,0.5 m)
L=1 m
ρ_s = ρ_f = 1 kg/m^3
μ_s = μ_f = 0.01 N·s/m^2
R=0.2 m
wall
L=1 m

Fig. 5

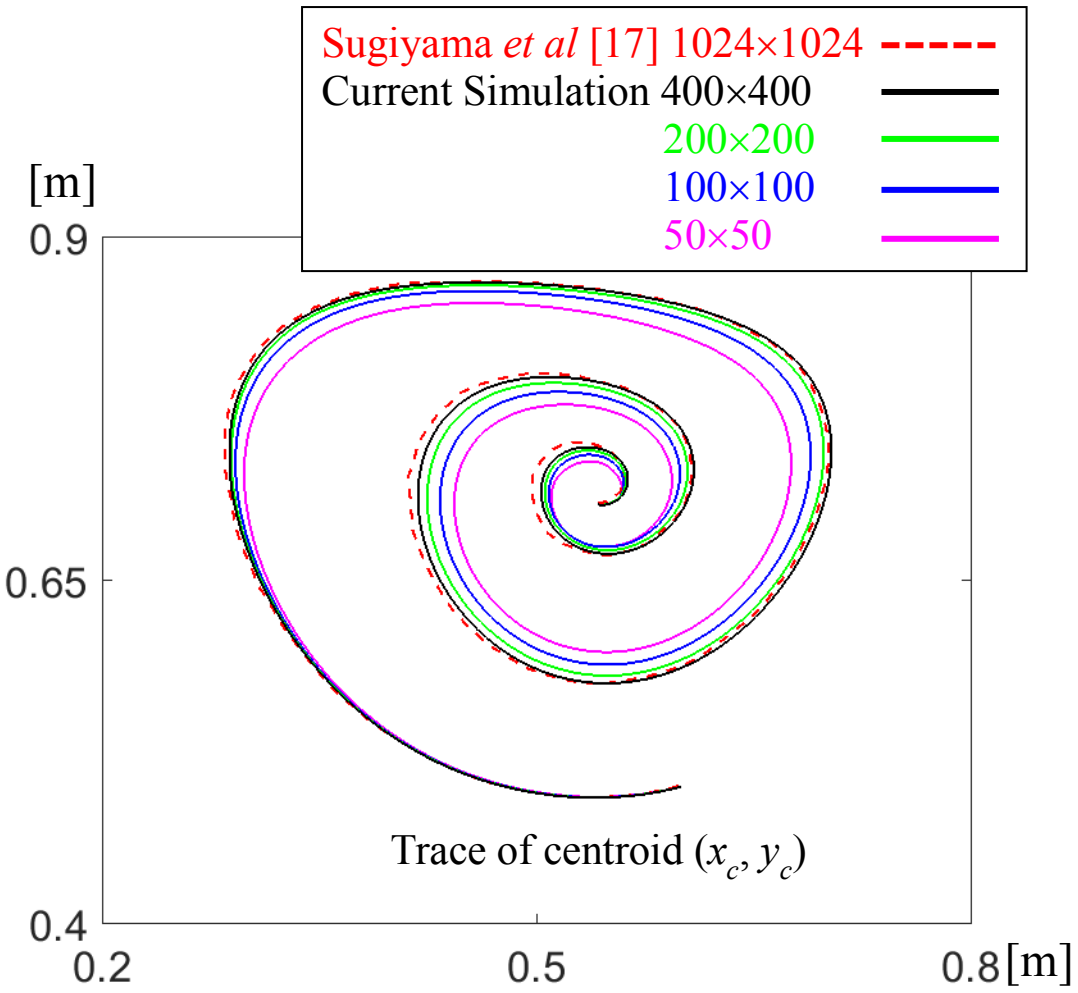
Sugiyama *et al* [17] 1024×1024
Current Simulation 400×400
200×200
100×100
50×50
[m]
0.9
0.65
0.4
0.2
0.5
0.8
[m]
Trace of centroid (x_c, y_c)

(a)

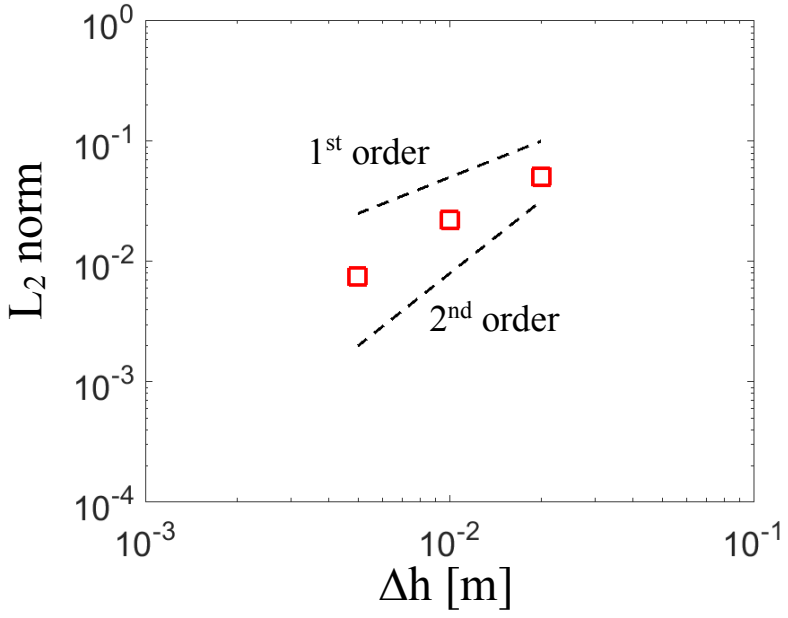
10^0
10^{-1}
10^{-2}
10^{-3}
10^{-4}
L_2 norm
1st order
2nd order
10^{-3}
10^{-2}
10^{-1}
Δh [m]

(b)

Fig. 6

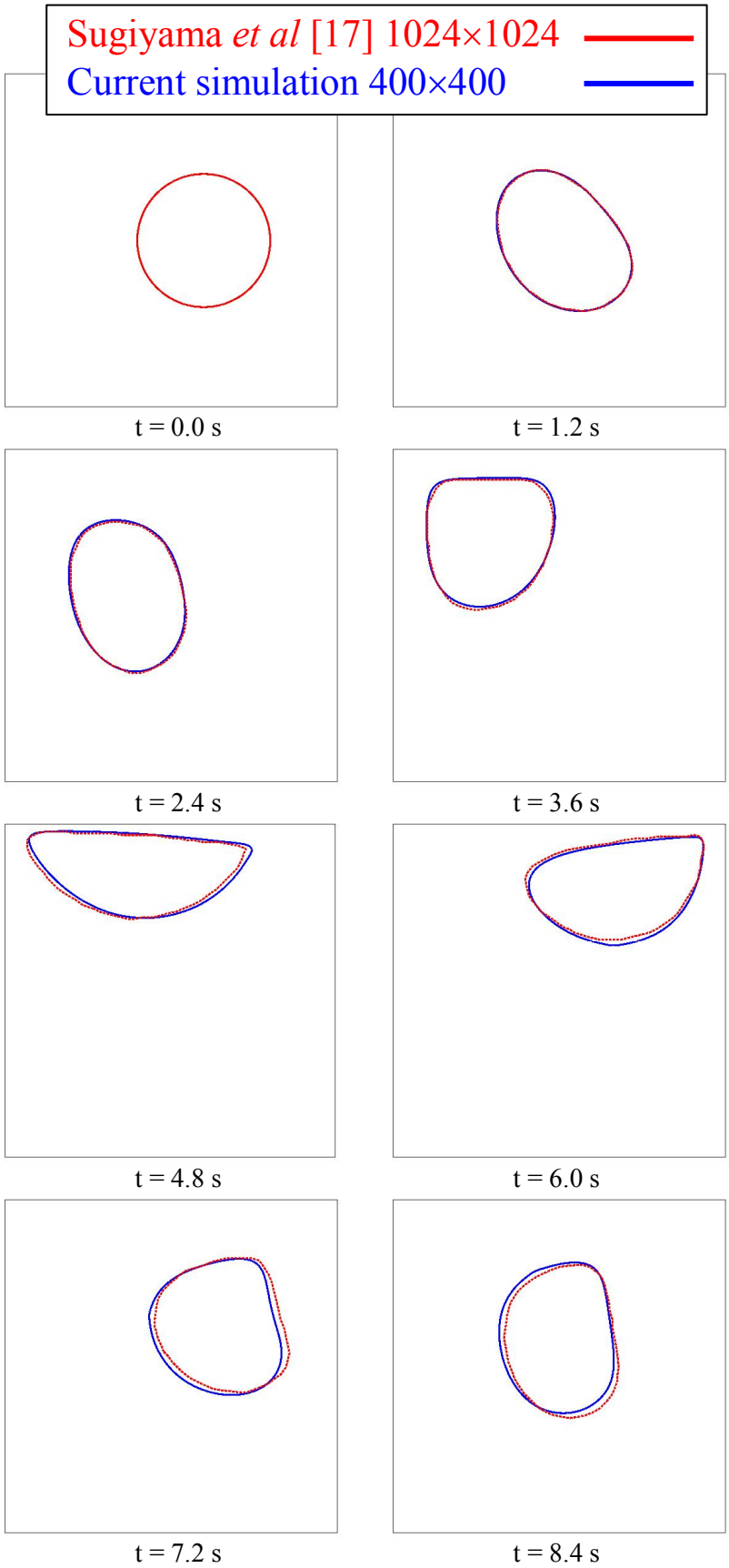
Sugiyama *et al* [17] 1024×1024
Current simulation 400×400
t = 0.0 s
t = 1.2 s
t = 2.4 s
t = 3.6 s
t = 4.8 s
t = 6.0 s
t = 7.2 s
t = 8.4 s

Fig. 7

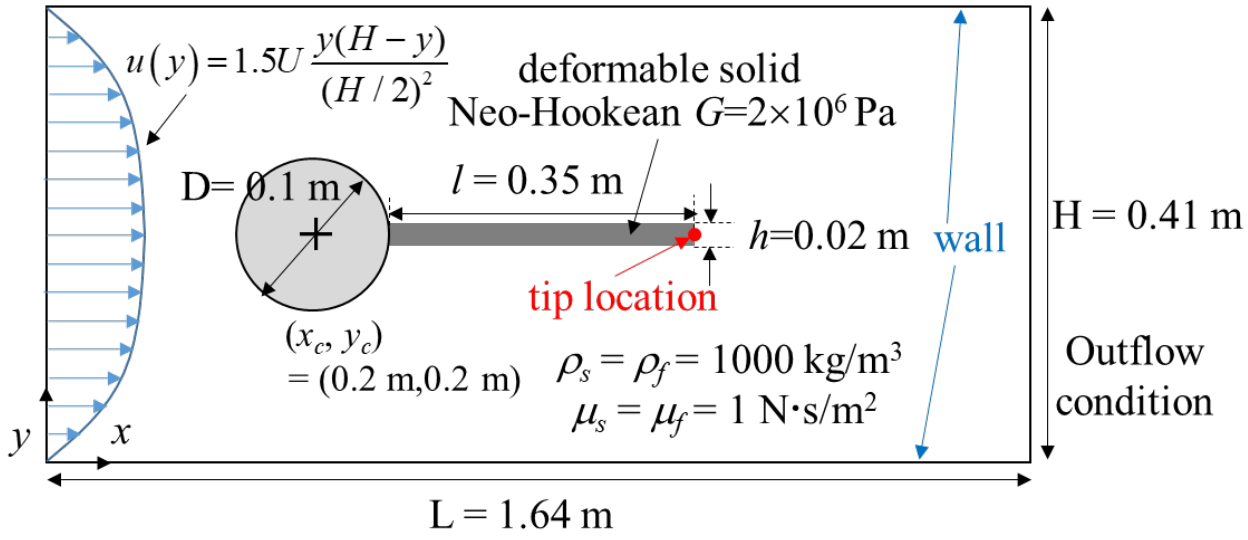
$u(y) = 1.5U \frac{y(H-y)}{(H/2)^2}$
deformable solid
Neo-Hookean G=2×10⁶ Pa
D= 0.1 m
l = 0.35 m
h=0.02 m
wall
H = 0.41 m
tip location
(x_c, y_c)
= (0.2 m,0.2 m)
$\rho_s = \rho_f$ = 1000 kg/m³
$\mu_s = \mu_f$ = 1 N·s/m²
Outflow
condition
y
x
L = 1.64 m

(a)

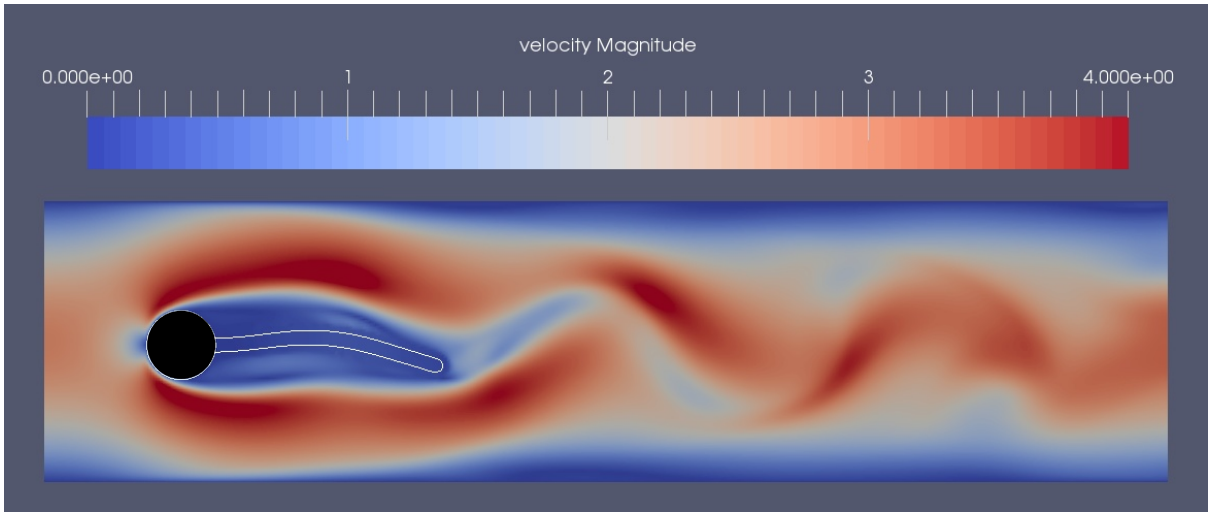
velocity Magnitude
0.000e+00
1
2
3
4.000e+00

(b)

Fig. 8

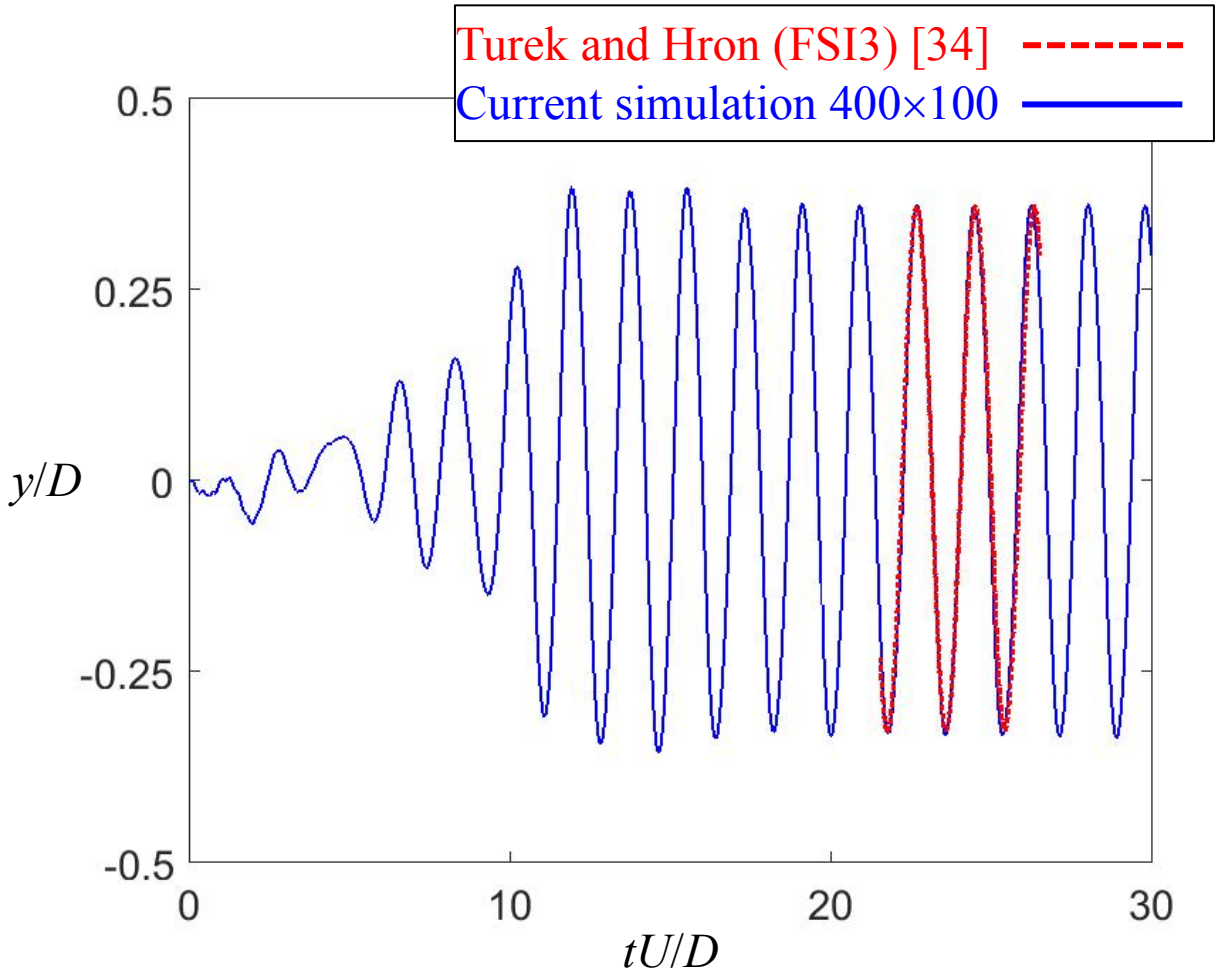
Turek and Hron (FSI3) [34]
Current simulation 400×100
0.5
0.25
0
-0.25
-0.5
y/D
0
10
20
30
tU/D

Fig. 9

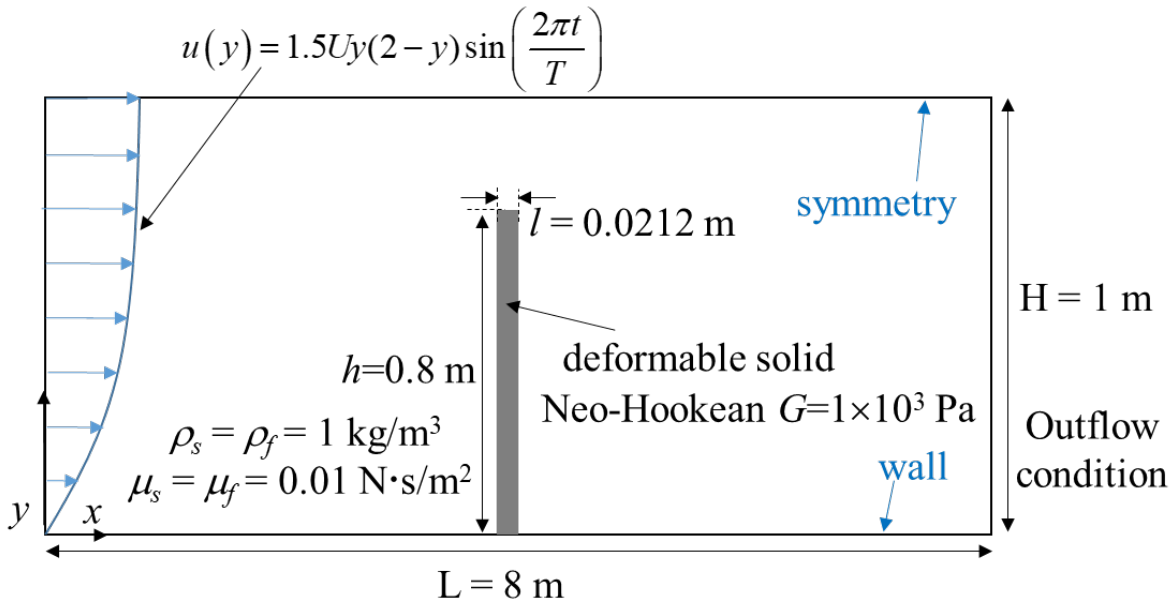
$u(y) = 1.5Uy(2-y)\sin\left(\frac{2\pi t}{T}\right)$
$l = 0.0212$ m
symmetry
H = 1 m
deformable solid
Neo-Hookean G=1×10³ Pa
h=0.8 m
$\rho_s = \rho_f = 1$ kg/m³
$\mu_s = \mu_f = 0.01$ N·s/m²
Outflow condition
wall
y
x
L = 8 m

Fig. 10

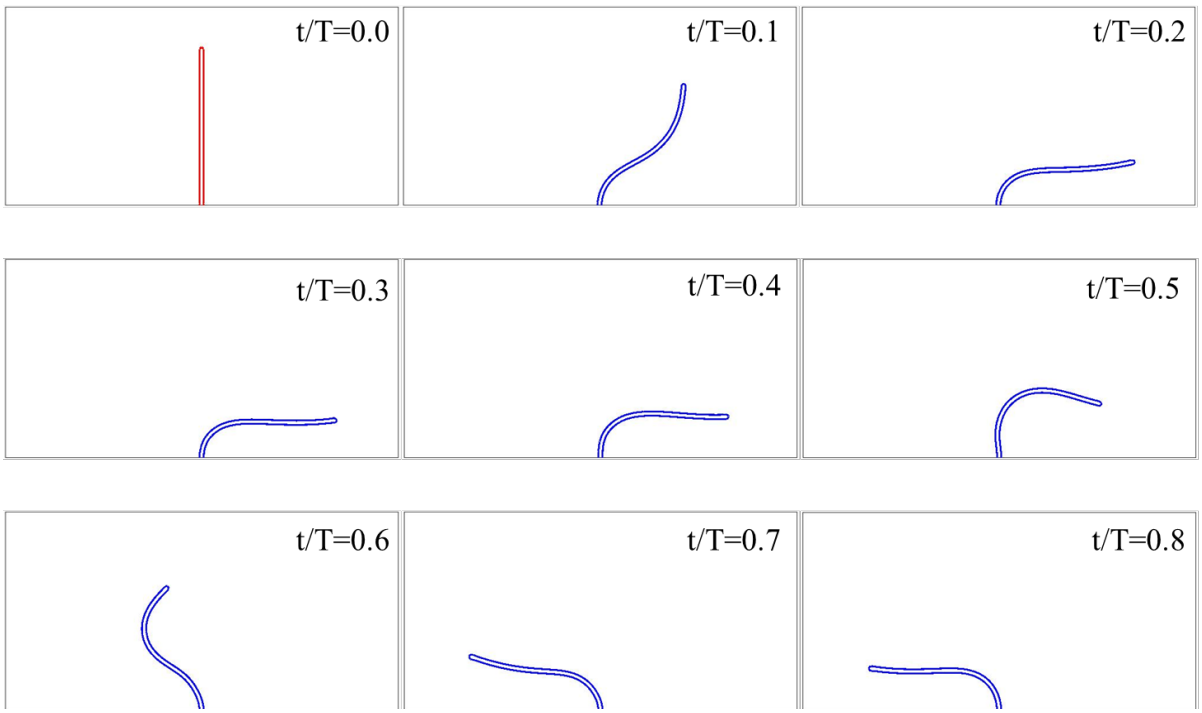

Fig. 11

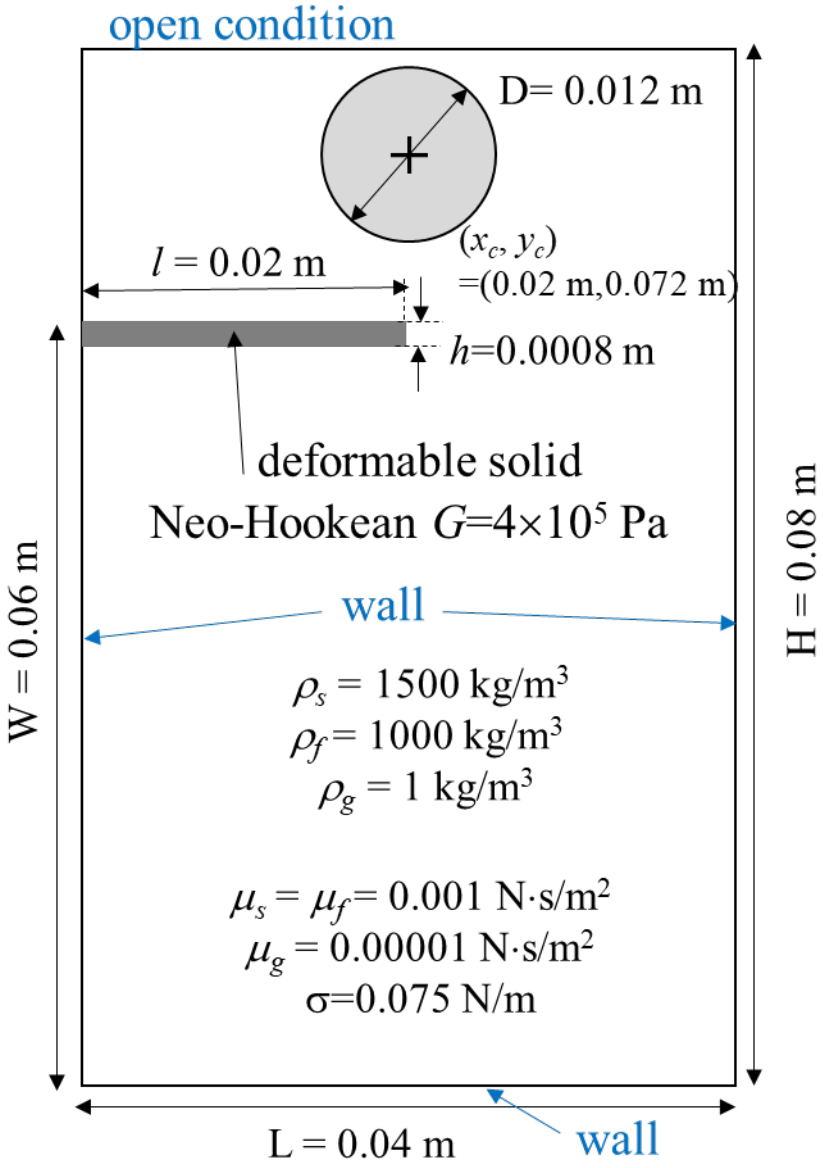
open condition
D= 0.012 m
(x_c, y_c)
=(0.02 m,0.072 m)
l = 0.02 m
h=0.0008 m
deformable solid
Neo-Hookean G=4×10^5 Pa
wall
ρ_s = 1500 kg/m^3
ρ_f = 1000 kg/m^3
ρ_g = 1 kg/m^3
μ_s = μ_f = 0.001 N·s/m^2
μ_g = 0.00001 N·s/m^2
σ=0.075 N/m
W = 0.06 m
H = 0.08 m
L = 0.04 m
wall

Fig. 12

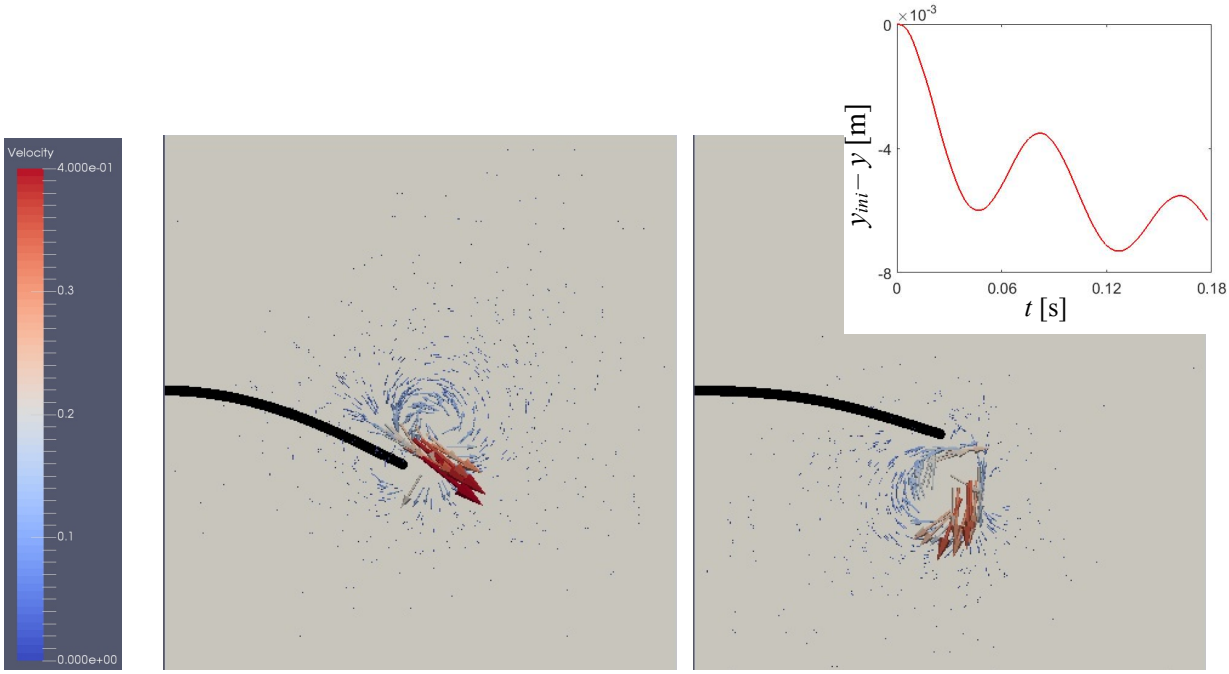

(a) t = 0.05 s (b) t = 0.08 s

(c) t = 0.12 s (d) t = 0.16 s

Fig. 13

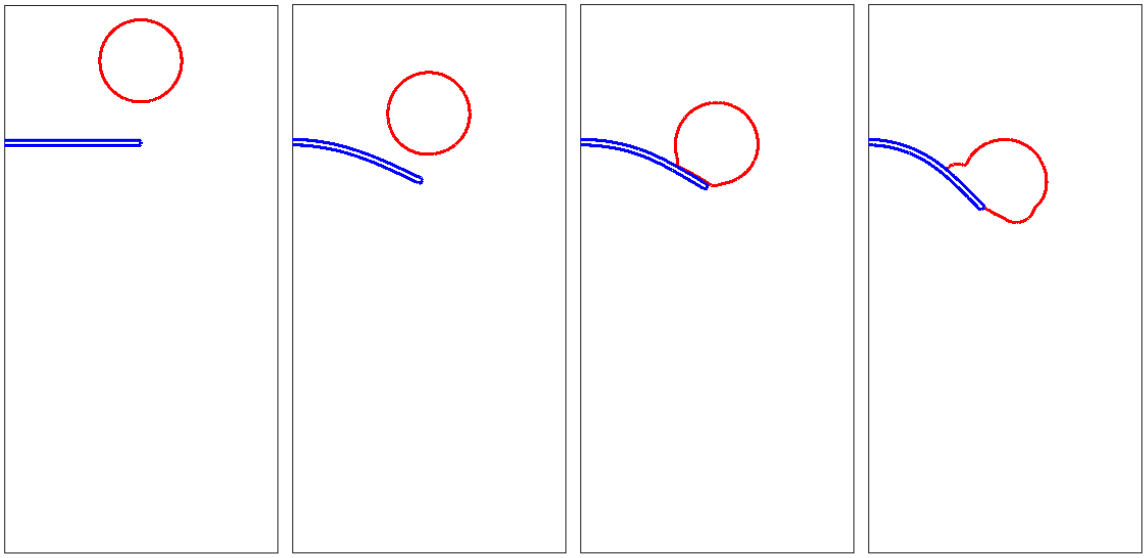

(a) t =0 s (b) t = 0.04 s (c) t = 0.05 s (d) t=0.06 s

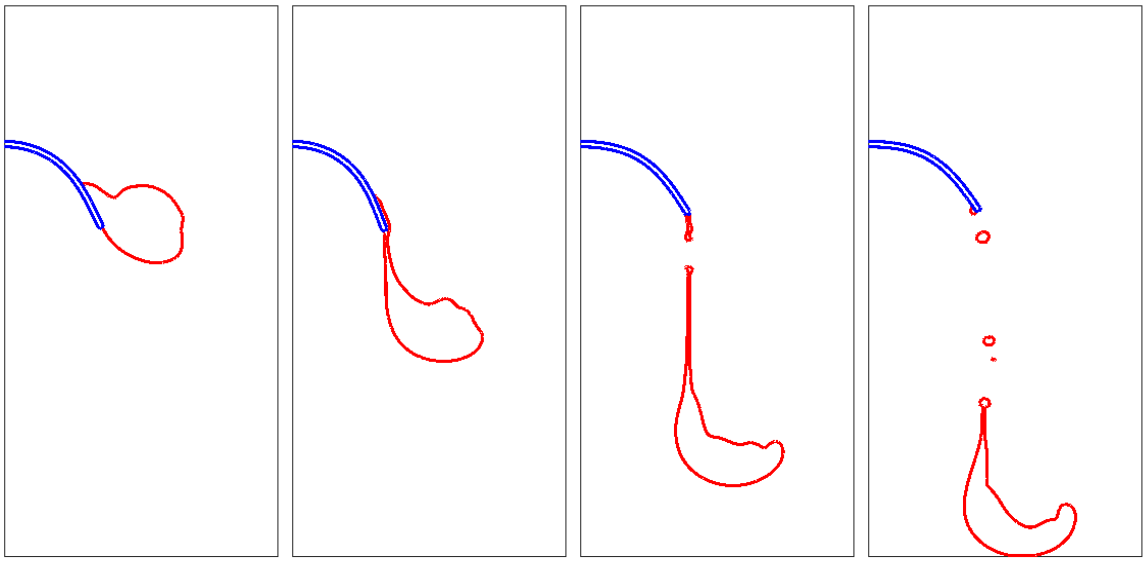

(e) t =0.07 s (f) t = 0.09 s (g) t = 0.11 s (h) t=0.12 s

Fig. 14

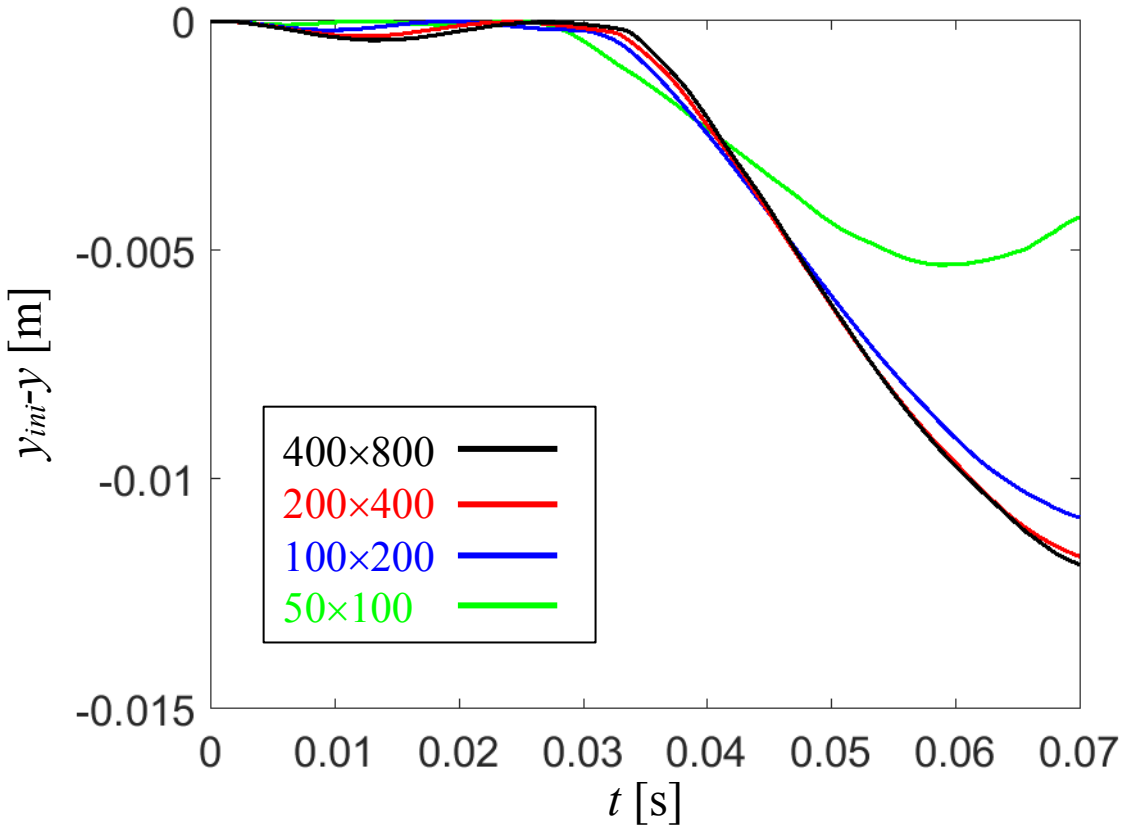
0
-0.005
-0.01
-0.015
y_{ini}-y [m]
0
0.01
0.02
0.03
0.04
0.05
0.06
0.07
t [s]
400×800
200×400
100×200
50×100

Fig. 15

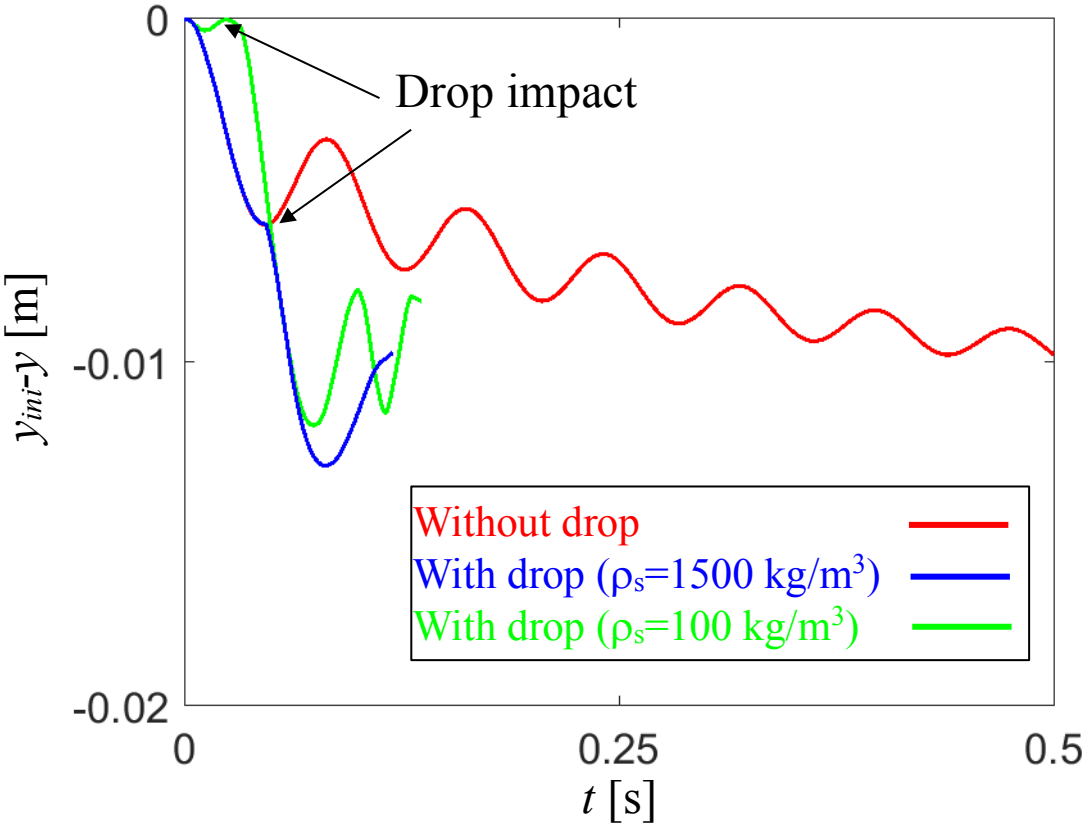
0
-0.01
-0.02
0
0.25
0.5
y_{ini}-y [m]
t [s]
Drop impact
Without drop
With drop (ρ_s=1500 kg/m^3)
With drop (ρ_s=100 kg/m^3)

Fig. 16

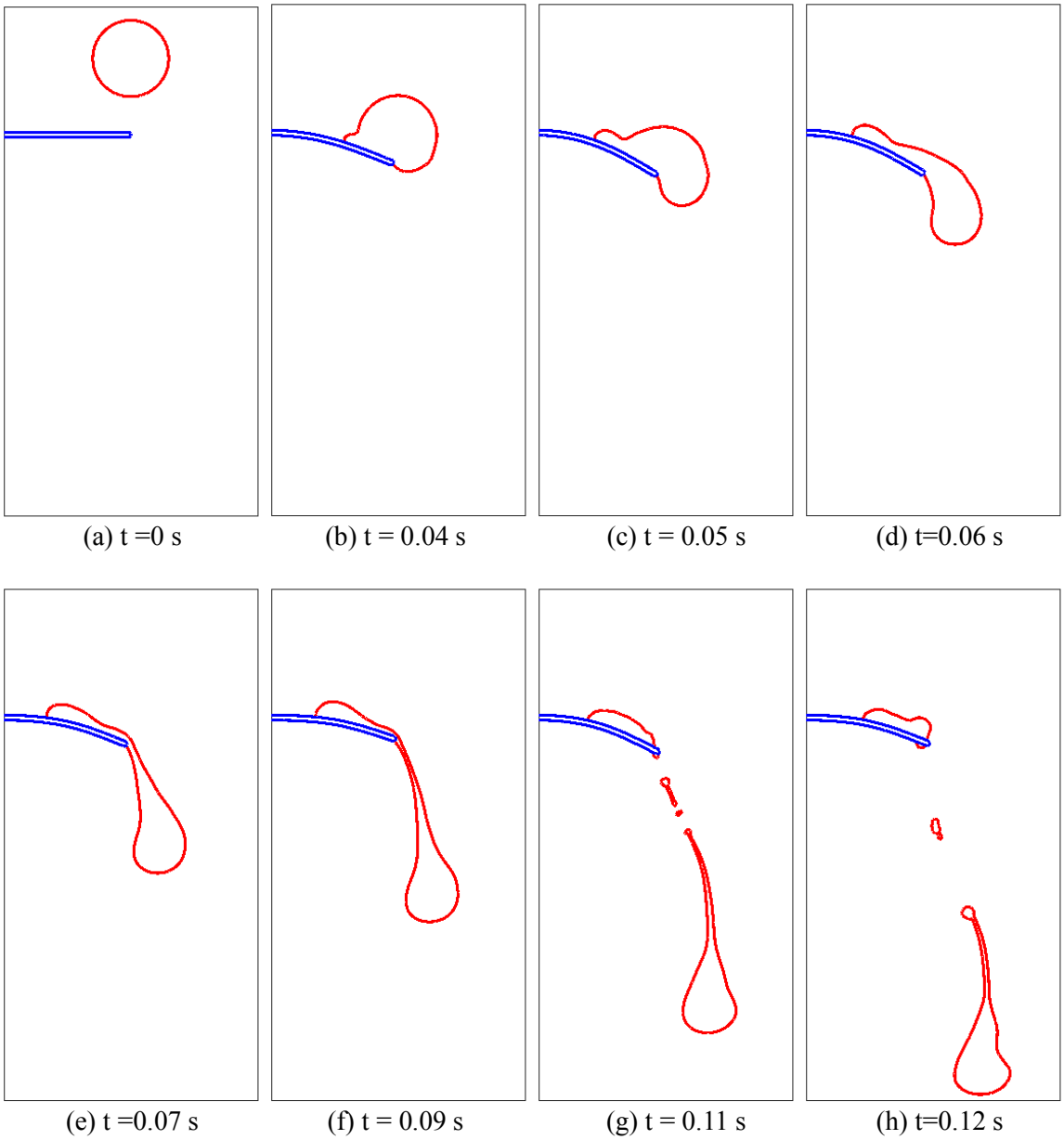

(a) t =0 s (b) t = 0.04 s (c) t = 0.05 s (d) t=0.06 s

(e) t =0.07 s (f) t = 0.09 s (g) t = 0.11 s (h) t=0.12 s

Fig. 17

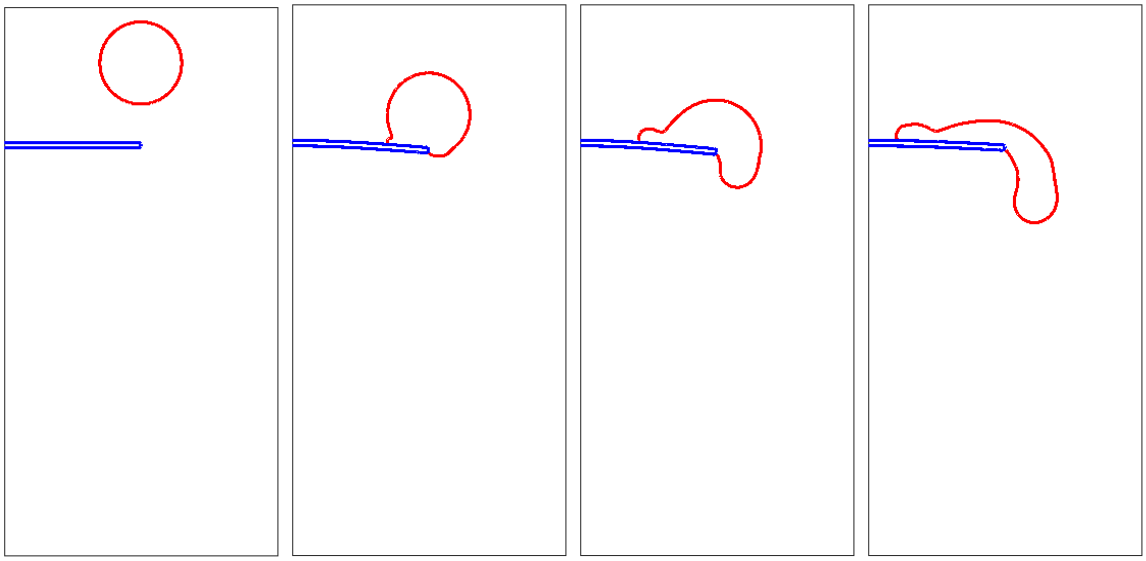

(a) t =0 s (b) t = 0.04 s (c) t = 0.05 s (d) t=0.06 s

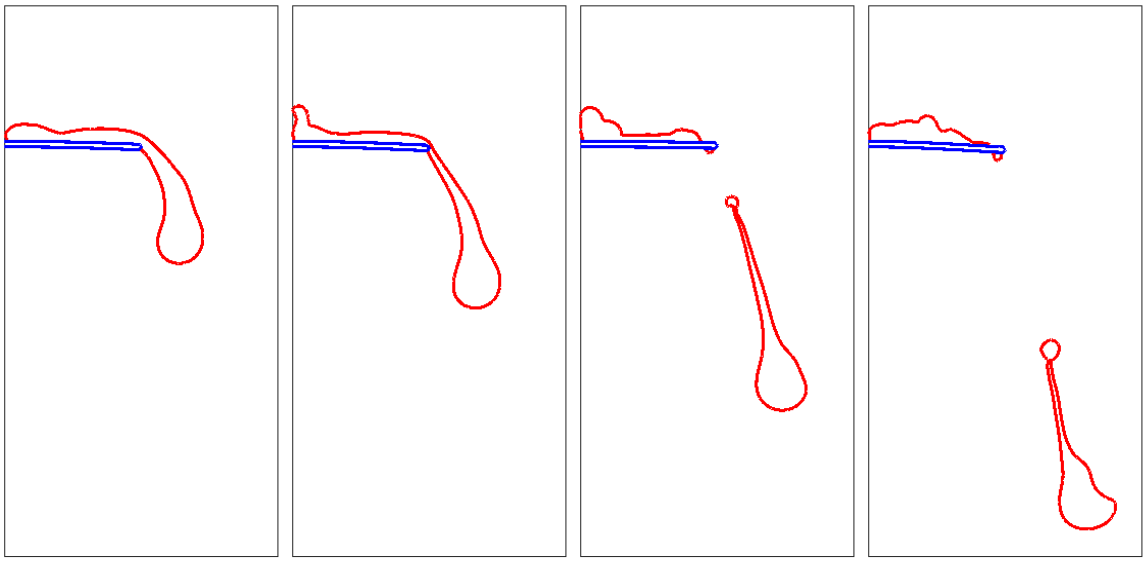

(e) t =0.07 s (f) t = 0.09 s (g) t = 0.11 s (h) t=0.12 s

Fig. 18

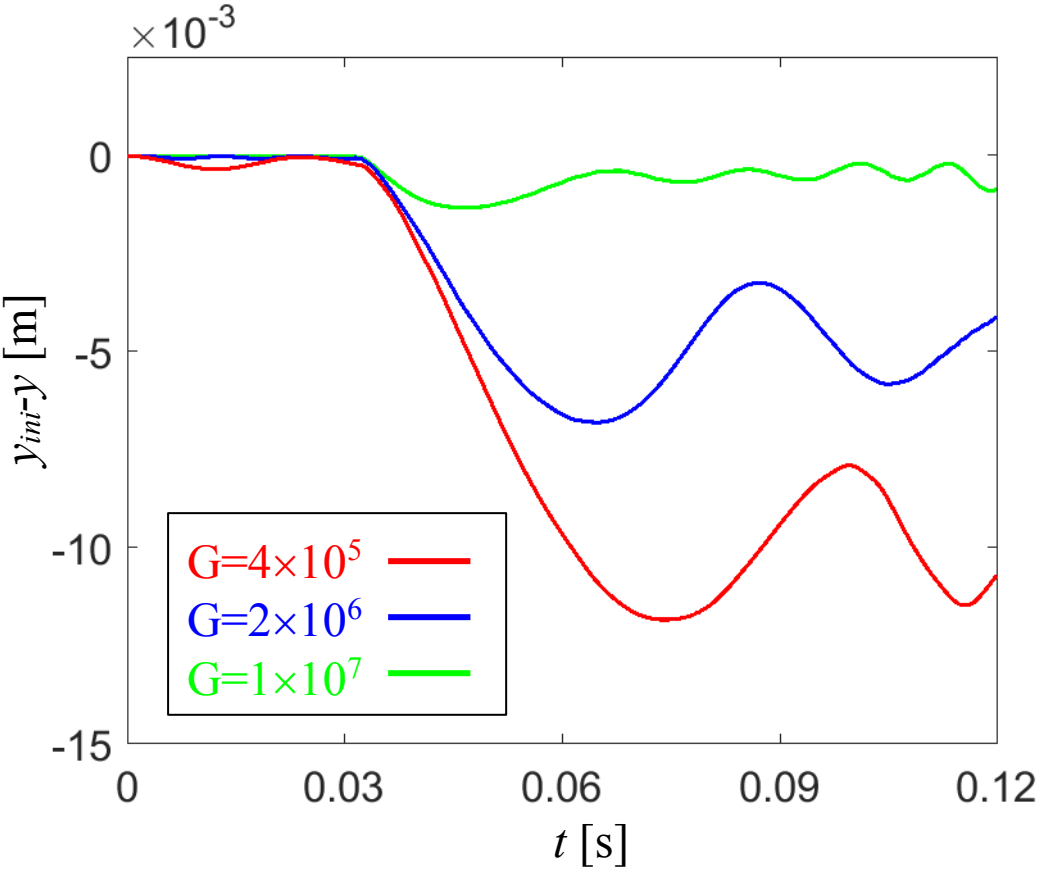

Fig. 19

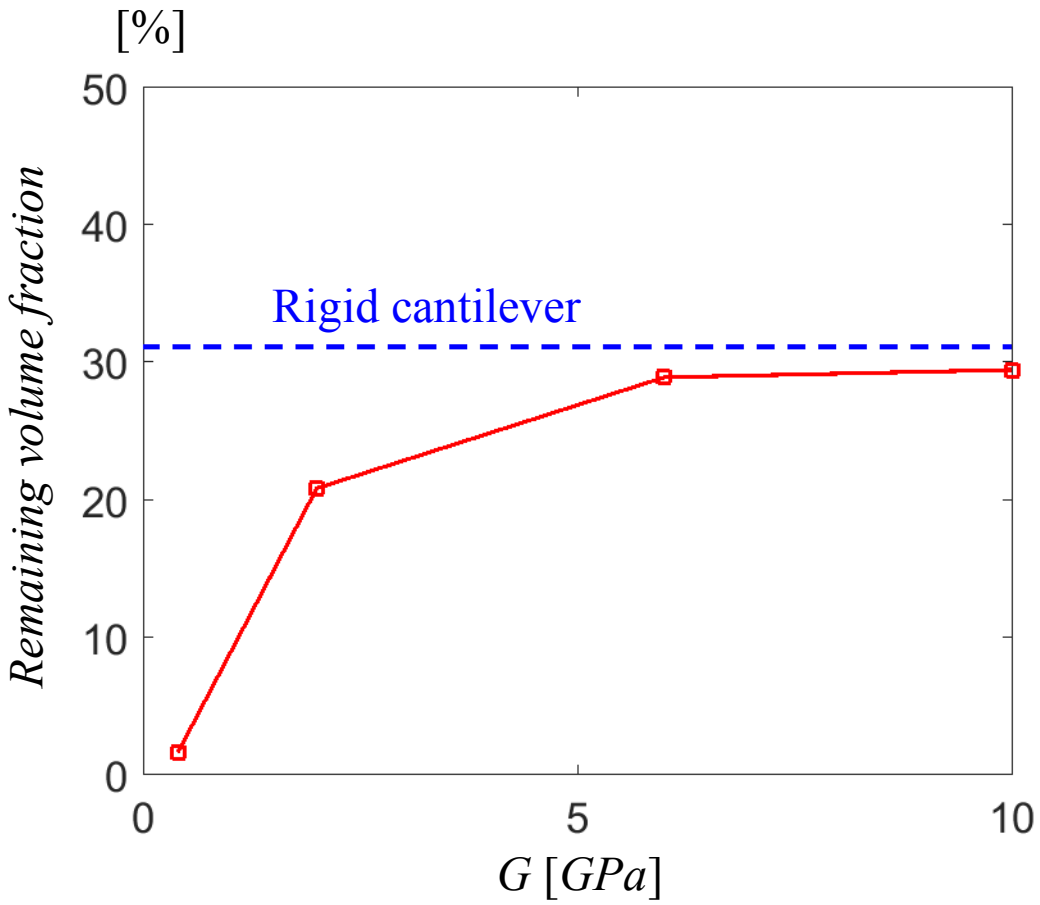
[%]
50
40
30
20
10
0
Remaining volume fraction
Rigid cantilever
0
5
10
G [GPa]

Fig. 20

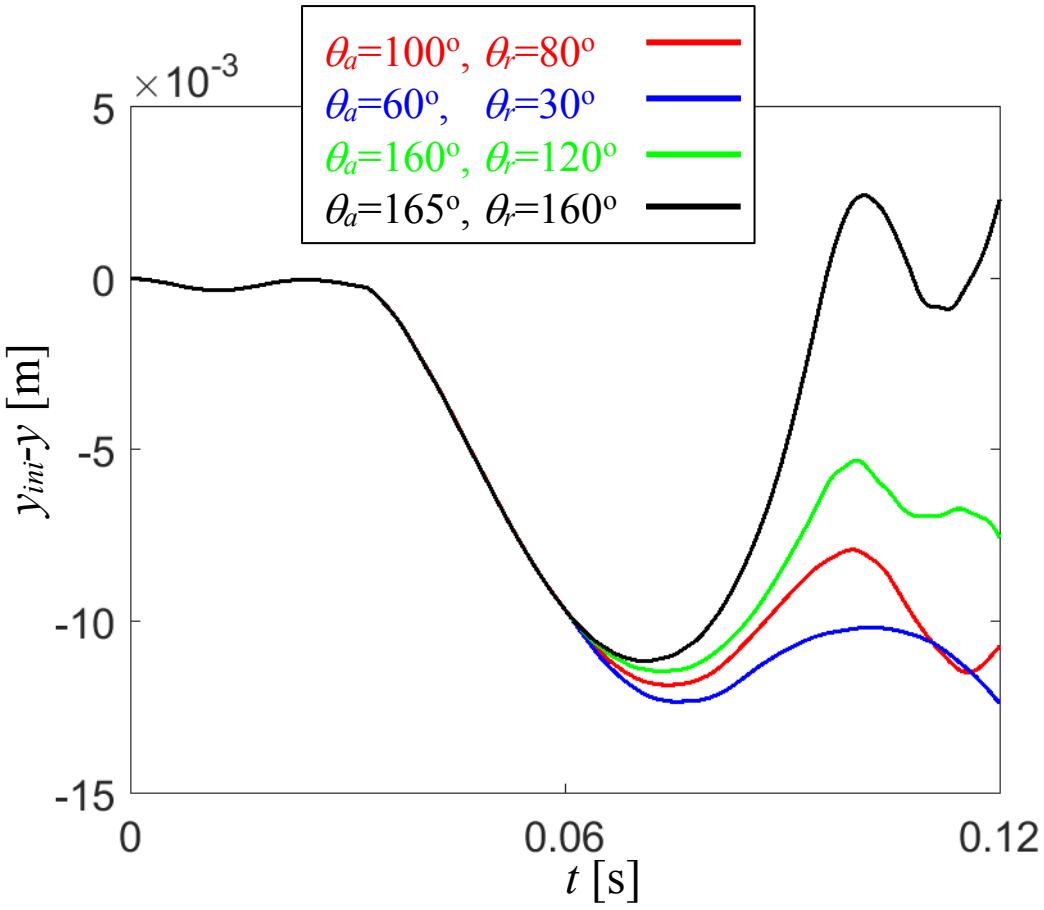
θa=100°, θr=80°
θa=60°, θr=30°
θa=160°, θr=120°
θa=165°, θr=160°
×10-3
5
0
-5
-10
-15
yini-y [m]
0
0.06
0.12
t [s]

Fig. 21

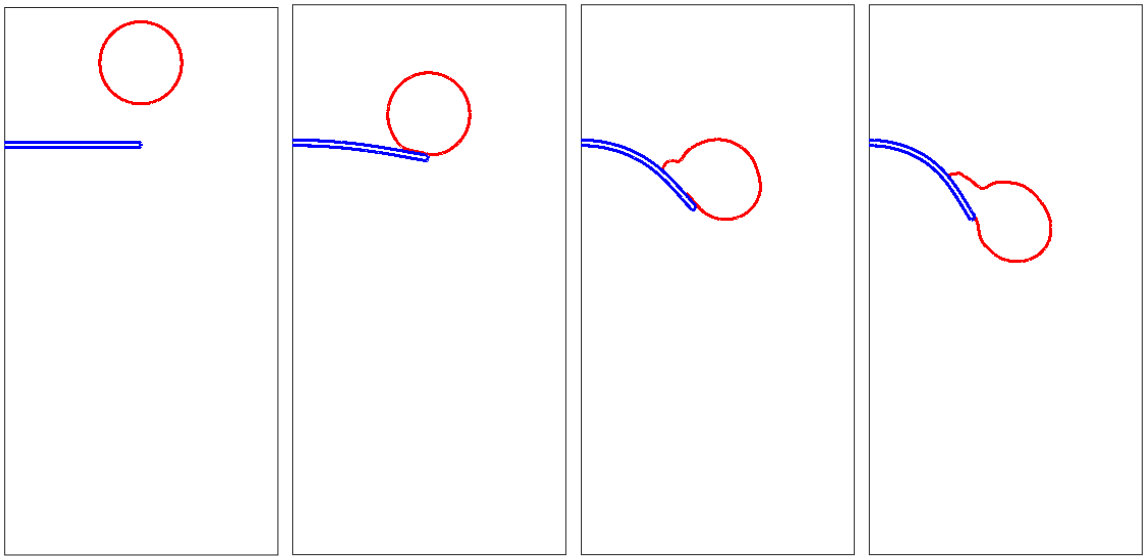

(a) t =0 s (b) t = 0.04 s (c) t = 0.06 s (d) t=0.07 s

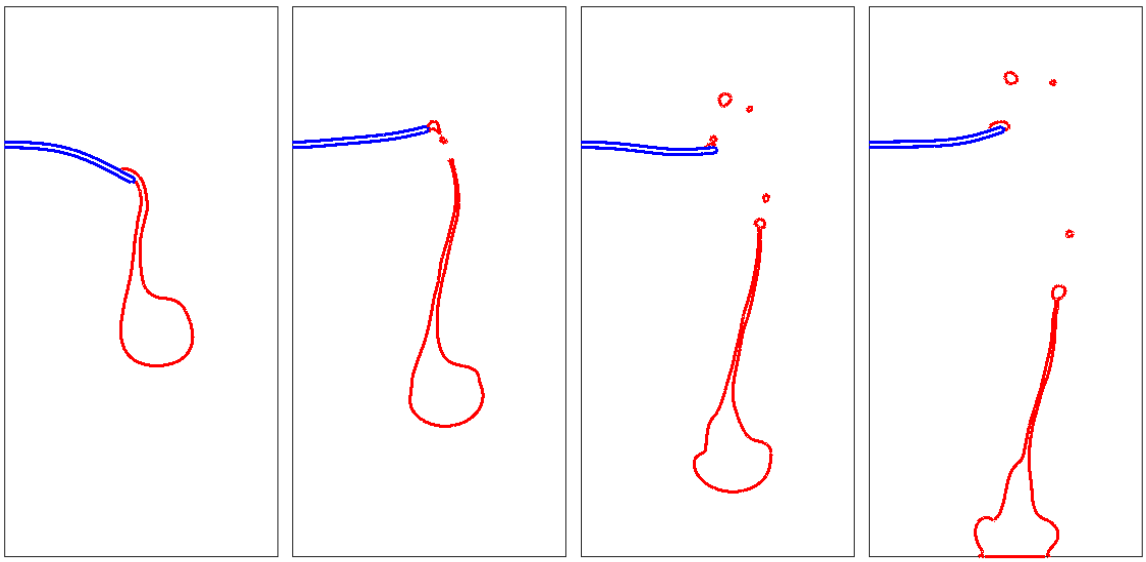

(e) t =0.09 s (f) t = 0.10 s (g) t = 0.11 s (h) t=0.12 s

Fig. 22

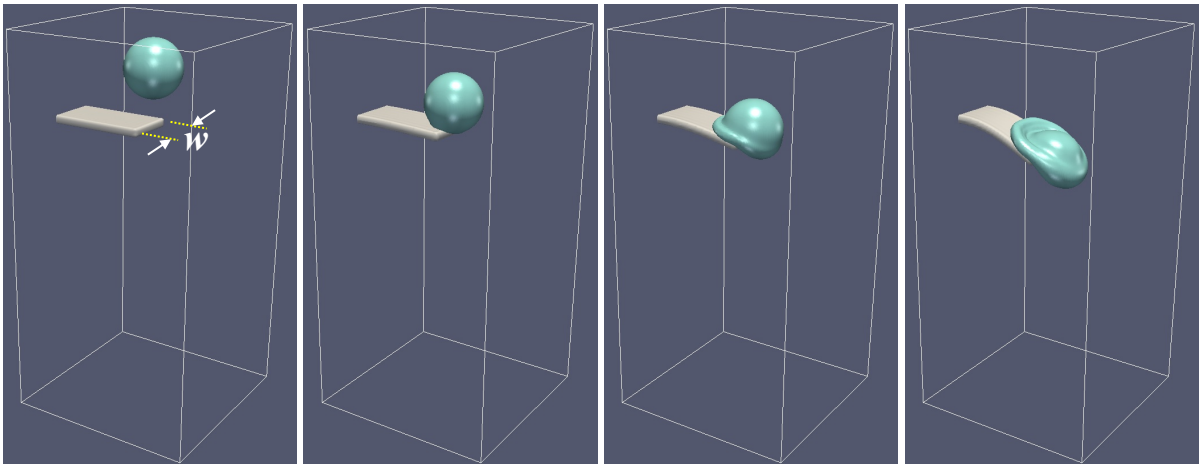

(a) t =0.0 s (b) t = 0.0375 s (c) t = 0.05 s (d) t=0.0625 s

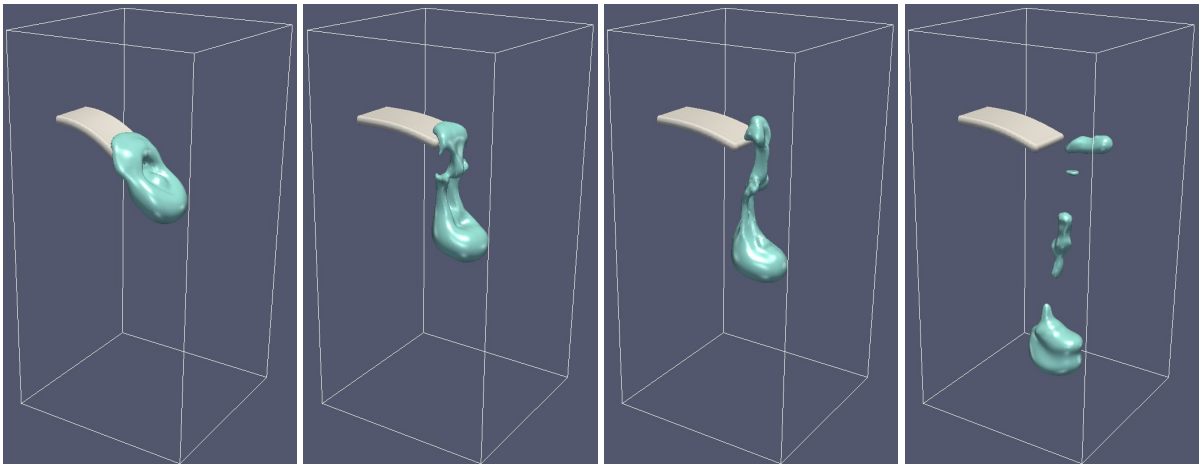

(e) t =0.075 s (f) t = 0.0875 s (g) t = 0.0938 s (h) t=0.1188 s

Fig. 23

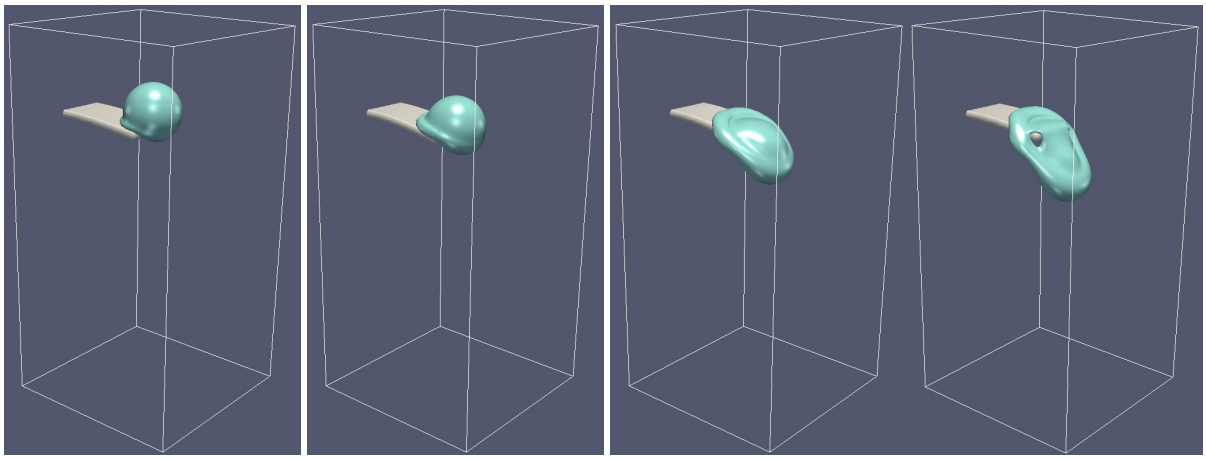

(a) t =0.0438 s (b) t = 0.05 s (c) t = 0.0625 s (d) t=0.0688 s

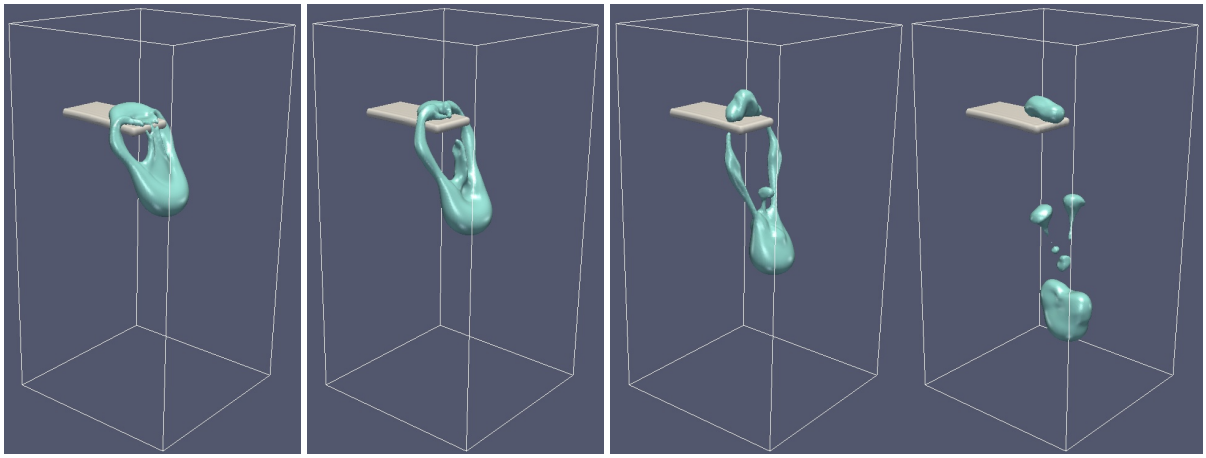

(e) t =0.075 s (f) t = 0.0813 s (g) t = 0.0938 s (h) t=0.1125 s

Fig. 24

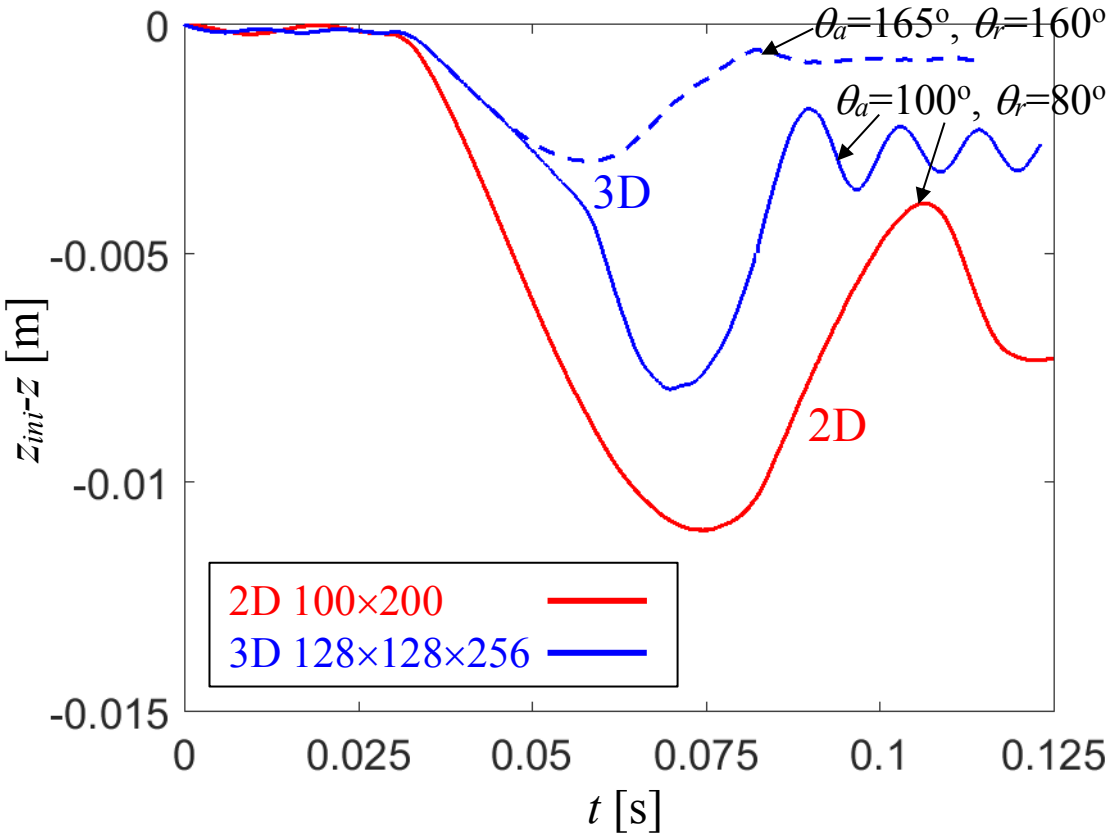
0
-0.005
-0.01
-0.015
0
0.025
0.05
0.075
0.1
0.125
z_{ini}-z [m]
t [s]
θ_a=165°, θ_r=160°
θ_a=100°, θ_r=80°
3D
2D
2D 100×200
3D 128×128×256

Fig. 25

APPENDIX

Our 3D grid structure shown in Fig. A1 uses a conventional staggered arrangement (as in 2D). The pressure, distance function, and diagonal terms for the strain field (B_{xx}, B_{yy}, B_{zz}) are located at cell centers. The x, y, and z components of the velocity field are located at cell faces. Off-diagonal terms for the strain field (B_{xy}, B_{yz}, B_{xz}) are placed at the grid node points in their corresponding cross-sectional plane (see Fig. A1)

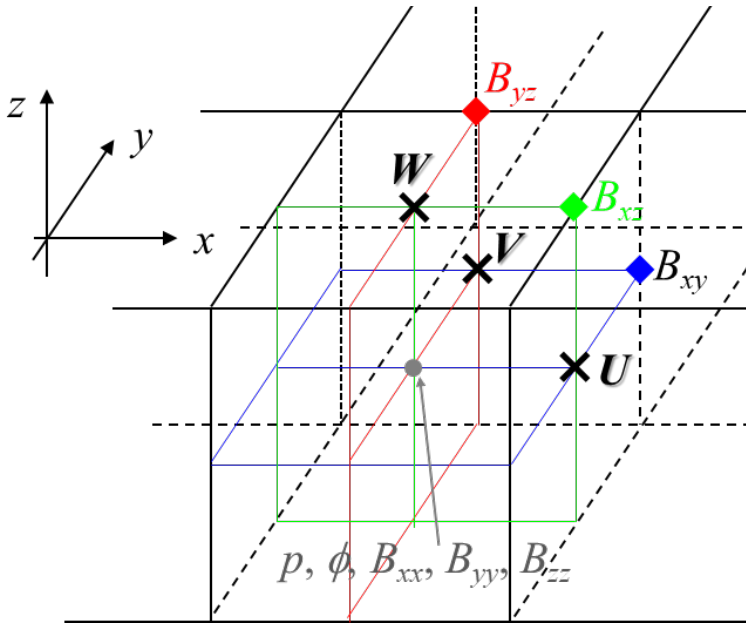

Fig. A1 Grid structure for 3D variables

The three-dimensional left Cauchy-Green strain tensor can be written as:

$$\mathbf{B} = \mathbf{F} \cdot \mathbf{F}^T = \begin{pmatrix} \frac{\partial x}{\partial X} & \frac{\partial x}{\partial Y} & \frac{\partial x}{\partial Z} \\ \frac{\partial y}{\partial X} & \frac{\partial y}{\partial Y} & \frac{\partial y}{\partial Z} \\ \frac{\partial z}{\partial X} & \frac{\partial z}{\partial Y} & \frac{\partial z}{\partial Z} \end{pmatrix} \begin{pmatrix} \frac{\partial x}{\partial X} & \frac{\partial y}{\partial X} & \frac{\partial z}{\partial X} \\ \frac{\partial x}{\partial Y} & \frac{\partial y}{\partial Y} & \frac{\partial z}{\partial Y} \\ \frac{\partial x}{\partial Z} & \frac{\partial y}{\partial Z} & \frac{\partial z}{\partial Z} \end{pmatrix} \tag{A1}$$

where (x,y,z) is the current and (X,Y,Z) is the reference or original location of the material. Again we

are not computing the deformation tensor, **F**, instead we are evaluating the **B** field transport equation directly. In 3D, we define a modified left Cauchy-Green strain tensor, **C**, (slightly differently than is done in Eq. (7)) :

$$\mathbf{C} = H_s^{1/3}\mathbf{B} \tag{A2}$$

Thus Eq. (8) becomes:

$$\tilde{\boldsymbol{\sigma}} == \left[\mu_f + (\mu_s - \mu_f)H_s\right]\left(\nabla\mathbf{u} + \nabla\mathbf{u}^T\right) + H_s\tilde{\boldsymbol{\sigma}}_{sh} = \mu\left(\nabla\mathbf{u} + \nabla\mathbf{u}^T\right) + GH_s^{2/3}\mathbf{C} \tag{A3}$$

The full 3D transport equation for the left Cauchy-Green strain field can be written as:

$$\begin{aligned}
&\frac{\partial B_{xx}}{\partial t} + u_s\frac{\partial B_{xx}}{\partial x} + v_s\frac{\partial B_{xx}}{\partial y} + w_s\frac{\partial B_{xx}}{\partial z} = 2\frac{\partial u_s}{\partial x}B_{xx} + 2\frac{\partial u_s}{\partial y}B_{xy} + 2\frac{\partial u_s}{\partial z}B_{xz}\\
&\frac{\partial B_{yy}}{\partial t} + u_s\frac{\partial B_{yy}}{\partial x} + v_s\frac{\partial B_{yy}}{\partial y} + w_s\frac{\partial B_{yy}}{\partial z} = 2\frac{\partial v_s}{\partial x}B_{xy} + 2\frac{\partial v_s}{\partial y}B_{yy} + 2\frac{\partial v_s}{\partial z}B_{yz}\\
&\frac{\partial B_{zz}}{\partial t} + u_s\frac{\partial B_{zz}}{\partial x} + v_s\frac{\partial B_{zz}}{\partial y} + w_s\frac{\partial B_{zz}}{\partial z} = 2\frac{\partial w_s}{\partial x}B_{xz} + 2\frac{\partial w_s}{\partial y}B_{yz} + 2\frac{\partial w_s}{\partial z}B_{zz}\\
&\frac{\partial B_{xy}}{\partial t} + u_s\frac{\partial B_{xy}}{\partial x} + v_s\frac{\partial B_{xy}}{\partial y} + w_s\frac{\partial B_{xy}}{\partial z} = \frac{\partial v_s}{\partial x}B_{xx} + \frac{\partial u_s}{\partial y}B_{yy} - \frac{\partial w_s}{\partial z}B_{xy} + \frac{\partial u_s}{\partial z}B_{yz} + \frac{\partial v_s}{\partial z}B_{xz}\\
&\frac{\partial B_{yz}}{\partial t} + u_s\frac{\partial B_{yz}}{\partial x} + v_s\frac{\partial B_{yz}}{\partial y} + w_s\frac{\partial B_{yz}}{\partial z} = \frac{\partial w_s}{\partial y}B_{yy} + \frac{\partial v_s}{\partial z}B_{zz} + \frac{\partial w_s}{\partial x}B_{xy} - \frac{\partial u_s}{\partial x}B_{yz} + \frac{\partial v_s}{\partial x}B_{xz}\\
&\frac{\partial B_{xz}}{\partial t} + u_s\frac{\partial B_{xz}}{\partial x} + v_s\frac{\partial B_{xz}}{\partial y} + w_s\frac{\partial B_{xz}}{\partial z} = \frac{\partial w_s}{\partial x}B_{xx} + \frac{\partial u_s}{\partial z}B_{zz} + \frac{\partial w_s}{\partial y}B_{xy} + \frac{\partial u_s}{\partial y}B_{yz} - \frac{\partial v_s}{\partial y}B_{xz}
\end{aligned} \tag{A4}$$

Equation (A4) can be solved using the semi-Lagrangian advection method as described in the 2D case. The incompressibility condition for 3D becomes:

$$\begin{aligned}
\det(\mathbf{C}) = {} & C_{xx}C_{yy}C_{zz} + C_{xy}C_{yz}C_{xz} + C_{xz}C_{xy}C_{yz}\\
& - C_{xz}C_{yy}C_{xz} - C_{xx}C_{yz}C_{yz} - C_{xy}C_{xy}C_{zz} = H_s
\end{aligned} \tag{A5}$$

Similar to the discussion for Eq. (25), this determinant, as calculated in the simulation, will in general not be equal to H_s but some other value H_c. Thus, we modify the **C** field by dividing by $\sqrt[3]{H_s / H_c}$.